CrossMark

J. Fluid Mech. (2018), *vol.* 845, *pp.* 642–681. © Cambridge University Press 2018
doi:10.1017/jfm.2018.255

Thin films in partial wetting: stability, dewetting and coarsening

A. Alizadeh Pahlavan[1], L. Cueto-Felgueroso[1], A. E. Hosoi[1], G. H. McKinley[1] and R. Juanes[1,†]

[1]Massachusetts Institute of Technology, Cambridge, MA 02139, USA

(Received 11 August 2017; revised 10 January 2018; accepted 18 March 2018; first published online 27 April 2018)

A uniform nanometric thin liquid film on a solid substrate can become unstable due to the action of van der Waals (vdW) forces. The instability leads to dewetting of the uniform film and the formation of drops. To minimize the total free energy of the system, these drops coarsen over time until one single drop remains. Here, using a thermodynamically consistent framework, we derive a new model for thin films in partial wetting with a free energy that resembles the Cahn–Hilliard form with a height-dependent surface tension that leads to a generalized disjoining pressure, and revisit the dewetting problem. Using both linear stability analysis and nonlinear simulations we show that the new model predicts a slightly smaller critical instability wavelength and a significantly (up to six-fold) faster growth rate than the classical model in the spinodal regime; this faster growth rate brings the theoretical predictions closer to published experimental observations. During coarsening at intermediate times, the dynamics become self-similar and model-independent; we therefore observe the same scalings in both the classical (with and without thermal noise) and new models. Both models also lead to a mean-field Lifshitz–Slyozov–Wagner (LSW)-type droplet-size distribution at intermediate times for small drop sizes. We, however, observe a skewed drop-size distribution for larger drops in the new model; while the tail of the distribution follows a Smoluchowski equation, it is not associated with a coalescence-dominated coarsening, calling into question the association made in some earlier experiments. Our observations point to the importance of the height dependence of surface tension in the early and late stages of dewetting of nanometric films and motivate new high-resolution experimental observations to guide the development of improved models of interfacial flows at the nanoscale.

Key words: contact lines, interfacial flows (free surface), thin films

1. Introduction

Understanding the underlying physics of how fluids coat solid substrates has been a long-standing quest in fluid dynamics (Blake & Ruschak 1979; Ruschak 1985; Quéré 1999; Weinstein & Ruschak 2004; Snoeijer & Andreotti 2013). With the advent of micro and nanoscale lithography techniques enabling manipulation at increasingly small scales (Xia & Whitesides 1998; Gates *et al.* 2005; Qin, Xia &

† Email address for correspondence: juanes@mit.edu

https://doi.org/10.1017/jfm.2018.255 Published online by Cambridge University Press

Whitesides 2010), and with applications ranging from micro/nanofluidics to additive manufacturing (Stone, Stroock, & Ajdari 2004; Schoch, Han & Renaud 2008; Wijshoff 2010; Kumar 2015), questions arise regarding the relevant description of fluid physics at the nanoscale and the validity of continuum modelling at such small scales (Squires & Quake 2005; Bocquet & Charlaix 2010; Colin, Squires & Bocquet 2012; Bocquet & Tabeling 2014; Lohse & Zhang 2015). As the thickness of a liquid film on a solid substrate becomes smaller than approximately 100 nm, the atoms at the liquid–solid and liquid–gas interfaces start interacting with each other, giving rise to additional intermolecular forces that need to be considered in continuum modelling (Rauscher & Dietrich 2008; Bonn *et al.* 2009; Israelachvili 2011).

A uniform nanometric thin liquid film on a solid substrate can become unstable due to these intermolecular forces. The instability leads to dewetting of the film and the formation of drops. Both liquid and solid-state dewetting at the nanoscale are relevant in many phenomena (Blossey 2012; Gentili *et al.* 2012; Thompson 2012; Mukherjee & Sharma 2015; Pierre-Louis 2016) such as pumping liquids using nanowires (Huang *et al.* 2013), patterning via self-assembly (Gau *et al.* 1999; Higgins & Jones 2000; Lopes & Jaeger 2001; Huang *et al.* 2005; Segalman 2005; van Hameren *et al.* 2006; Pokroy *et al.* 2009; Fowlkes *et al.* 2011; Han & Lin 2012; Thiele 2014; Kong *et al.* 2015, 2016; Wu *et al.* 2015), synthesis of core–shell nanoparticle arrays (McKeown *et al.* 2015), droplet generation (Yamamoto *et al.* 2015; Keiser *et al.* 2017), needle growth (Yu, Bulović & Hosoi 2013), understanding slip and rheology of nanometric films (Herminghaus, Seemann & Jacobs 2002; Fetzer *et al.* 2005, 2007*a*; Bäumchen & Jacobs 2010; Bäumchen *et al.* 2012; Bäumchen *et al.* 2014; McGraw *et al.* 2014), tear film dynamics (Braun 2012), film flow in heat pipes (Kundan *et al.* 2017), Rayleigh–Plateau instability of nanowires or liquids in nanochannels (Molares *et al.* 2004; Chen, Zhang & Russell 2007), or stability of bubbles/drops in micro/nanochannels (Huerre *et al.* 2015; Hammoud *et al.* 2017).

Reiter (1992, 1993) was the first to experimentally characterize the dewetting of a nanometric polymer film on a solid substrate. He observed that, initially, some holes form with a seemingly characteristic wavelength between them; these holes then expand with a ridge formed at the receding front; these ridges ultimately meet and form a network of polygonal patterns. The ridges later collapse due to the Rayleigh–Plateau instability, forming small droplets of approximately uniform size. On a much longer time scale still, these droplets can coarsen to ultimately form a single drop; the time scale associated with this last stage, however, is very long and not readily accessible within typical experiments.

The theory for instability of thin liquid films under the influence of intermolecular forces far predates the experimental observations, dating back to Vrij (1966), Sheludko (1967), Ruckenstein & Jain (1974), Williams & Davis (1982), Wyart & Daillant (1990), Brochard-Wyart, Martin & Redon (1993), Sharma & Reiter (1996), Sharma & Khanna (1998) and Oron (2000). The Navier–Stokes equations describing the fluid motion can be greatly simplified using the long-wave/lubrication approximation when the characteristic lateral length of the flow is much larger than its characteristic height, an approach that has its origins in the work of Reynolds to describe the pressure distribution for slider bearings (Reynolds 1886). For ultrathin liquid films, an additional disjoining pressure term arises due to the intermolecular interactions between the solid–liquid and liquid–gas interfaces.

Assuming a particular form for the intermolecular forces, one can use linear stability analysis of the thin-film equation to arrive at a prediction for the scaling of the wavelength of the instability and its growth rate as a function of the initial

https://doi.org/10.1017/jfm.2018.255 Published online by Cambridge University Press

uniform film thickness (Oron, Davis & Bankoff 1997; Craster & Matar 2009); this regime predicted by the linear theory is known as the spinodal regime. In apolar systems, typically van der Waals (vdW) forces are the main long-range attractive interactions, scaling with the film thickness as $\sim 1/h^2$, leading to a scaling of $\sim h^2$ and $\sim 1/h^5$ for the most unstable wavelength and fastest growth rate, respectively. These scalings therefore serve as a qualitative benchmark for the experiments to determine if they are within the spinodal regime. Making quantitative predictions, however, requires prescribing the exact form of the interface potential.

The observations by Reiter (1992, 1993) led to a wave of experimental studies focusing on dewetting of thin liquid films. Jacobs, Herminghaus & Mecke (1998) showed that the holes observed in the experiments of Reiter (1992, 1993) have a Poisson distribution, a signature of the nucleation regime, and that the scaling of the film-rupture time as a function of film thickness did not match the theoretical predictions of the spinodal regime; films in the nucleation regime are linearly stable, yet instabilities can still grow due to the presence of defects on the substrate or in the film itself (Jacobs *et al.* 1998). The first observations of the spinodal regime were reported by Bischof *et al.* (1996) and Herminghaus *et al.* (1998) using thin gold films on quartz substrates, where the correlations between the holes was rigorously shown using Minkowski functionals (Mecke 1998; Mantz, Jacobs & Mecke 2008).

The presence of residual stresses in thin polymer films can further complicate the dewetting process; Reiter *et al.* (2005) observed dewetting through nucleation for large film thicknesses, where the film is expected to be linearly stable. They realized that the number of holes is a strong function of the ageing time of the polymer before the temperature is raised above the glass transition temperature to perform the experiments; they further speculated that the reason behind this observation could be that during the spin-coating process, the solvent evaporates quickly, leaving the polymer chains in non-equilibrium configurations leading to a residual stress in the film, which can be responsible for the unexpected instability of the films. The observations by Reiter *et al.* (2005) therefore point to the need for extreme caution in conducting and interpreting experiments on thin films in spinodal and nucleation regimes (Stange, Evans & Hendrickson 1997; Thiele, Mertig & Pompe 1998; Xie *et al.* 1998; Segalman & Green 1999; Meredith *et al.* 2000; Bollinne *et al.* 2003; Sharma 2003; Nguyen *et al.* 2014).

Seemann, Herminghaus & Jacobs (2001*a*) conducted a series of well-controlled experiments using polystyrene films spin-cast on silicon (Si) wafers. They demonstrated that by tuning the thickness of the silicon oxide coating of the Si wafer, they could alter the interface potential and classify three categories of instabilities: (1) spinodal dewetting for linearly unstable regions, (2) thermal nucleation at the edge of the linearly unstable region, where thermal fluctuations can overcome the energy barrier leading to dewetting, and (3) heterogeneous nucleation within the linearly stable region, where defects on the substrate or in the film give rise to the appearance of holes and instabilities. The spinodal regime is easily distinguishable as it gives rise to a well-defined characteristic wavelength of instability, from which the interface potential can be reconstructed. The key feature distinguishing regimes 2 and 3 is that holes continuously appear throughout the experiment in the thermal nucleation regime, whereas they all form within a limited time window in the heterogeneous nucleation regime.

Becker *et al.* (2003) observed good agreement between experimental observations and theoretical predictions, with the caveat that experiments showed a faster rupture time. To explain the time-scale mismatch between theory and experiments,

https://doi.org/10.1017/jfm.2018.255 Published online by Cambridge University Press

Mecke & Rauscher (2005), Grün, Mecke & Rauscher (2006) and Fetzer *et al.* (2007*b*) suggested that accounting for thermal fluctuations is necessary. They showed that thermal noise at the typical temperatures used in the experiments can speed up the initial rupture process, thereby bringing the theoretical predictions closer to the experimental observations.

Here, we revisit the theory of thin liquid films in partial wetting and show that the intermolecular forces in thin films give rise to a height-dependent surface tension. We show that the free energy of the system can be cast in the following form:

$$\Gamma = \int \left(f(h) + \frac{1}{2}\kappa(h)(h_x)^2 \right) \mathrm{d}x, \tag{1.1}$$

which resembles the Cahn–Hilliard framework for phase separation in binary alloys (Cahn & Hilliard 1958; Langer 1971), an idea that dates back to van der Waals (Rowlinson 1979; Rowlinson & Widom 2013). Here, $f(h)$ is the bulk free energy and $\kappa(h)$ is a height-dependent surface tension term; this feature has important consequences for stability of liquid films, leading to a slightly smaller wavelength of instability and a faster rupture rate than the classical theory (by up to six times), bringing the theory closer to the experimental observations, and suggesting that the height dependence of surface tension could play a role along with the presence of thermal noise.

Within the framework of non-equilibrium thermodynamics (Hohenberg & Halperin 1977; Cross & Hohenberg 1993; Bray 2002), our model in non-dimensional form can be written succinctly as follows (Pahlavan *et al.* 2015):

$$\frac{\partial h}{\partial t} = \frac{\partial}{\partial x}\left(\mathcal{M} \frac{\partial}{\partial x}\left(\frac{\delta \Gamma}{\delta h} \right) \right), \tag{1.2}$$

with the mobility $\mathcal{M}$, and the pressure defined as the variational derivative of the free energy as $\tilde{P} = \delta\Gamma/\delta h = \mathrm{d}f/\mathrm{d}h - \sqrt{\kappa}\partial/\partial x(\sqrt{\kappa}\partial h/\partial x)$; here, h represents the height of the liquid film, κ is the height-dependent surface tension, and f is the bulk free energy.

Our model leads to a generalized form of the disjoining pressure defined as:

$$\Phi(h, h_x, h_{xx}) = \frac{\mathrm{d}\phi_{\mu,1}}{\mathrm{d}h} + \sqrt{\phi_{\mu,2}}\frac{\partial}{\partial x}\left(\sqrt{\phi_{\mu,2}}\frac{\partial h}{\partial x} \right), \tag{1.3}$$

with $\phi_{\mu,1}(h)$ and $\phi_{\mu,2}(h)$ as components of the vdW force. As indicated in (1.3), this generalized disjoining pressure depends not only on the film height, but also on its slope and curvature. This model allows describing the spreading and dewetting of drops and thin films in the true partial-wetting regime (Brochard-Wyart *et al.* 1991; de Gennes, Brochard-Wyart & Quéré 2004) without the need to invoke a precursor film (Pahlavan *et al.* 2015).

Using the new thin-film model, we revisit the instability and dewetting of a partially wetting thin liquid film on a solid substrate. We first analyse the equilibrium film and droplet solutions predicted by this model and contrast it with the classical model, showing that in our model the equilibrium droplets exhibit compact support and show a non-zero equilibrium angle at the contact line, whereas the classical thin-film model cannot admit solutions with compact support and the equilibrium droplet only asymptotically meets the substrate through a precursor film (Brenner & Bertozzi 1993). Analysing the stability of uniform film solutions, we show that

https://doi.org/10.1017/jfm.2018.255 Published online by Cambridge University Press

the new model predicts a faster growth rate and smaller wavelength of instability in the spinodal regime than the classical model. Upon dewetting, the newly formed liquid droplets arrive at a metastable state; they are connected by ultrathin fluid films of non-zero thickness and slowly coarsen to lower the energy of the system; this coarsening process, however, occurs on very long time scales as the dynamics is now mainly driven by drainage through the ultrathin films and the mobility scales as $\sim h^3$, leading to very small rates of mass transfer between the droplets. We show that the coarsening process arrives at a self-similar intermediate-asymptotic behaviour (Barenblatt 1996), which is independent of the details of the contact-line models and even in the presence of thermal fluctuations matches the existing predictions for the classical thin-film model (Glasner & Witelski 2003; Gratton & Witelski 2008, 2009). We, however, observe a skewed drop-size distribution for larger drops in the new model; while the long-tailed distribution follows a Smoluchowski equation, it is not associated with a coalescence-dominated coarsening process, calling into question the association made between coalescence and skewed drop-size distribution in some earlier experiments.

2. Thin-film model in partial wetting

2.1. *Free energy at equilibrium: emergence of Cahn–Hilliard framework with height-dependent surface tension*

Consider a nanometric thin liquid film sitting on a solid substrate, as shown in figure 1. When the film is perturbed, it can become unstable if the solid prefers to be in contact with the gas phase; in this configuration the uniform film has the lowest interfacial area, so dewetting lowers the bulk energy of the system at the expense of increasing its interfacial energy. We can write the energy of a half drop in one dimension as

$$\Gamma = \int_0^{x_0} \phi(h, h_x)\,\mathrm{d}x, \tag{2.1}$$

where ϕ is the free energy density, $x = 0$ marks the centre of the drop and $x = x_0$ is where the liquid, solid and gas meet, i.e. the contact line. At equilibrium, the variation of the free energy is zero, i.e. $\delta\Gamma = 0$:

$$\delta\left(\int_0^{x_0} (\phi(h, h_x) - Ph)\,\mathrm{d}x\right) = 0, \tag{2.2}$$

where the operator δ indicates variation of the functional and the Lagrange multiplier P is introduced to enforce mass conservation. Expanding the above equation leads to

$$\int_0^{x_0} \left(\frac{\partial\phi}{\partial h} - P\right)\delta h\,\mathrm{d}x + \int_0^{x_0} \frac{\partial\phi}{\partial h_x}\delta h_x\,\mathrm{d}x + \phi|_{x_0}\delta x_0 = 0. \tag{2.3}$$

Using integration by parts, we can rewrite the second integral in (2.3), leading to

$$\begin{aligned}\delta\int_0^{x_0} (\phi(h, h_x) - Ph)\,\mathrm{d}x \;=\; &\int_0^{x_0} \left[\frac{\partial\phi}{\partial h} - \frac{\mathrm{d}}{\mathrm{d}x}\left(\frac{\partial\phi}{\partial h_x}\right) - P\right]\delta h\,\mathrm{d}x \\ &+ \left(\frac{\partial\phi}{\partial h_x}\right)\delta h\Big|_0^{x_0} + \phi|_{x_0}\delta x_0 = 0.\end{aligned} \tag{2.4}$$

https://doi.org/10.1017/jfm.2018.255 Published online by Cambridge University Press

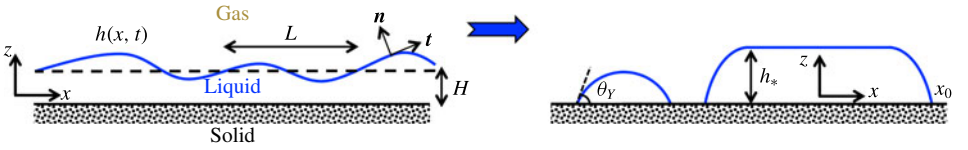


FIGURE 1. (Colour online) Schematic of a liquid film on a solid substrate; films with a height less than approximately 100 nm can become unstable to infinitesimal perturbations if the liquid does not completely wet the substrate; in such situations, the instabilities grow and the film dewets from the substrate, forming small droplets that can then coarsen to form larger drops; the shape of the small drops is governed mainly by surface tension, leading to a spherical cap shape with a macroscopic Young contact angle θ_Y; deviations from the spherical cap shape can occur due to the intermolecular forces very close to the contact line. If the height of the drop becomes comparable to the capillary length $l_\gamma = \sqrt{\gamma/(\rho g)}$, gravitational force becomes important, levelling the drop and forming a puddle shape; gravity sets the upper limit $h_* = 2l_\gamma \sin(\theta_Y/2)$ for the puddle height.

We can further use the Taylor expansion for the boundary terms and write $\delta h|_{x_0} = -\delta x_0(\partial h/\partial x)|_{x_0}$.

At equilibrium, the integrand as well as the boundary terms need to be independently zero. The integrand represents the Euler–Lagrange equation (Yeh, Newman & Radke 1999; Starov, Velarde & Radke 2007; Arfken, Weber & Harris 2013)

$$\left[\frac{\partial \phi}{\partial h} - \frac{\mathrm{d}}{\mathrm{d}x}\left(\frac{\partial \phi}{\partial h_x}\right)\right] = P. \tag{2.5}$$

The boundary condition at $x = x_0$ then becomes

$$-h_x\left(\frac{\partial \phi}{\partial h_x}\right)\bigg|_{x_0} + \phi|_{x_0} = 0. \tag{2.6}$$

This equation is known as the transversality condition or the Augmented Young equation. Note that the boundary terms at $x = 0$ automatically cancel out due to the symmetry conditions.

We therefore have two constraints on the free energy as we approach the contact line: (1) it should satisfy the Augmented Young equation (2.6), and (2) it should recover the solid–gas free energy at the contact line to allow for a continuous variation of the energy. Our objective therefore is to find the functional form of the free energy, whose minimizer at equilibrium satisfies these two conditions. Considering the macroscopic contributions to the free energy, i.e. gravity and interfacial energies, we can write the free energy as

$$\Gamma_M = \int_0^{x_0}\left(\frac{1}{2}\rho g h^2 + (\gamma_{sl} - \gamma_{sg}) + \gamma\sqrt{1 + h_x^2}\right)\mathrm{d}x, \tag{2.7}$$

where $\rho g h^2/2$ represents the gravitational potential energy, γ_{sl} and γ_{sg} represent the solid–liquid and solid–gas interfacial energies, and the term $\gamma\sqrt{1 + h_x^2}$ represents the liquid–gas interfacial energy contribution. Neglecting gravity, the Euler–Lagrange equation (2.5) will simplify to the usual Laplace equation for the pressure jump across an interface. We can now proceed to check whether the macroscopic free energy density satisfies the two constraints given above for equilibrium.

https://doi.org/10.1017/jfm.2018.255 Published online by Cambridge University Press

As the film height goes to zero, ϕ must be equal to the solid–gas interfacial energy; in the above representation of the free energy, we have subtracted this contribution, so we require $\phi(h=0)=0$. Therefore, as we move close to the contact line, we have $(\gamma_{sl}-\gamma_{sg})+\gamma\sqrt{1+h_x^2}|_{x_0}=0$. Here we consider the true partial-wetting regime, where a droplet is surrounded by a dry solid substrate. The same arguments can be applied for the case of pseudopartial wetting, where the droplet is surrounded by a precursor film of height h_f; in this case, the height at the contact line goes to h_f instead of zero.

The Augmented Young equation further requires the following:

$$-h_x\left(\gamma\frac{h_x}{\sqrt{1+h_x^2}}\right)\bigg|_{x_0}+\gamma\sqrt{1+h_x^2}\bigg|_{x_0}+(\gamma_{sl}-\gamma_{sg})=0. \tag{2.8}$$

Note that this equation can be simplified to give us the Young equation, i.e. $(\gamma_{sl}-\gamma_{sg})+(\gamma/\sqrt{1+h_x^2})|_{x_0}=0$, which in turn simplifies to $\gamma\cos\theta_Y=(\gamma_{sg}-\gamma_{sl})$, where θ_Y is the macroscopic Young contact angle (Young 1805).

Putting the Augmented Young equation and the continuity constraint together leads to the following conclusion:

$$\left(\gamma\frac{h_x^2}{\sqrt{1+h_x^2}}\right)\bigg|_{x_0}=0. \tag{2.9}$$

The only way for this equation to be satisfied is if $h_x(x_0)=0$; if we substitute $h_x(x_0)=0$ back in the Augmented Young equation, we arrive at $(\gamma_{sl}-\gamma_{sg})+\gamma=0$; using the Young equation, this leads to $\gamma(1-\cos\theta_Y)=0$, indicating that $\theta_Y=0$. In other words, the liquid needs to completely wet the surface for the constraints on the free energy to be satisfied. An alternative way of arriving at this conclusion is to consider a uniform flat film; the energy of this film is then written as $\int((1/2)\rho g h^2+(\gamma_{sl}-\gamma_{sg})+\gamma)\,\mathrm{d}x$; as we thin down the film and its height goes to zero, we need to recover the solid–gas interfacial energy, therefore we require $(\gamma_{sl}-\gamma_{sg})+\gamma=0$, which leads to the same result.

The macroscopic contributions to the free energy are therefore insufficient to model the partial-wetting regime; we need to incorporate the physics at the nanoscale close to the contact line. As the height of the liquid film becomes small, the liquid–solid and liquid–gas interfaces start to interact with each other, leading to an additional contribution in the free energy, commonly known as the disjoining pressure (de Gennes 1985). We can therefore write the free energy in the following form:

$$\Gamma=\Gamma_M+\Gamma_\mu=\int_0^{x_0}\left(\frac{1}{2}\rho g h^2+(\gamma_{sl}-\gamma_{sg})+\gamma\sqrt{1+h_x^2}+\phi_\mu(h)\right)\mathrm{d}x, \tag{2.10}$$

where $\phi_\mu(h)$ represents the intermolecular interactions close to the contact line. We now can check whether this form of the free energy satisfies the continuity constraint and the Augmented Young equation. The continuity of the free energy dictates

$$(\gamma_{sl}-\gamma_{sg})+\gamma\sqrt{1+h_x^2}\bigg|_{x_0}+\phi_\mu(h=0)=0. \tag{2.11}$$

The Augmented Young equation leads to the following:

$$-h_x\left(\gamma\frac{h_x}{\sqrt{1+h_x^2}}\right)\bigg|_{x_0}+\gamma\sqrt{1+h_x^2}\bigg|_{x_0}+(\gamma_{sl}-\gamma_{sg})+\phi_\mu(h=0)=0. \tag{2.12}$$

https://doi.org/10.1017/jfm.2018.255 Published online by Cambridge University Press

This equation represents the so-called Derjaguin–Frumkin equation (Starov *et al.* 2007), relating the Young angle to the microscopic forces close to the contact line: $\gamma\cos\theta_Y = \gamma\cos\theta_\mu + \phi_\mu(h=0)$, where θ_μ represents the microscopic angle at the contact line and we have used $h_x|_{x_0} = \tan\theta_\mu$ and the Young equation $\gamma_{sg} - \gamma_{sl} = \gamma\cos\theta_Y$ (Yeh *et al.* 1999; Starov *et al.* 2007; Starov 2010). The above two constraints on continuity of the energy and the augmented Young equation lead to $h_x(x_0) = 0$, or $\theta_\mu = 0$. Putting $h_x(x_0) = 0$ back into either of the above equations leads to $\phi_\mu(h = 0) = \mathcal{S}$, where $\mathcal{S} \equiv \gamma_{sg} - \gamma_{sl} - \gamma$ is known as the spreading parameter. Therefore, we arrive at the conclusion that while the macroscopic Young angle (θ_Y) can be non-zero, the microscopic angle at the contact line (θ_μ) needs to be zero to satisfy the energetic constraints; this regime is commonly known as pseudopartial wetting, where a macroscopic liquid drop is surrounded by a microscopic precursor film (Heslot *et al.* 1990; Brochard-Wyart *et al.* 1991; Sharma 1993*b*). To describe the true partial-wetting regime, in which a liquid droplet sits on a dry surface without a precursor film (de Gennes *et al.* 2004), additional physics is needed.

Surface tension at a liquid–gas interface arises due to the collective interactions between the liquid and gas molecules (Israelachvili 2011; Marchand *et al.* 2011). In the case of a uniform thin liquid film of nanometric thickness on a solid substrate, where liquid–gas and liquid–solid interfaces come very close to each other, the collective interactions also give rise to an excess free energy in addition to the interfacial tensions. For a nearly uniform thin film, this excess energy simply depends on the height of the film as represented by $\phi_\mu(h)$ (Israelachvili 2011). Close to the contact line, however, the interfaces are not parallel, and therefore the collective intermolecular interactions between solid, liquid and gas molecules lead to a slope-dependent excess free energy, i.e. $\phi_\mu(h, h_x)$ for a liquid wedge sitting on a solid substrate (Hocking 1993; Wu & Wong 2004; Dai, Leal & Redondo 2008). Using density functional theory, this excess free energy can be represented as a non-local integral of all the interactions (Keller & Merchant 1991; Merchant & Keller 1992; Getta & Dietrich 1998; Snoeijer & Andreotti 2008); however, here we use a simplified local approximation of the excess free energy, which has been shown to agree well with the non-local formulations (Bauer & Dietrich 1999; Bonn *et al.* 2009). We can therefore write the free energy as

$$\Gamma = \int_0^{x_0} \left(\frac{1}{2}\rho g h^2 + (\gamma_{sl} - \gamma_{sg}) + \gamma\sqrt{1 + h_x^2} + \phi_\mu(h, h_x) \right) \mathrm{d}x. \tag{2.13}$$

Continuity of the free energy leads to the following constraint at the contact line:

$$(\gamma_{sl} - \gamma_{sg}) + \gamma \left.\sqrt{1 + h_x^2}\right|_{x_0} + \phi_\mu(h, h_x)|_{x_0} = 0. \tag{2.14}$$

The augmented Young equation further becomes

$$-h_x \left(\gamma \frac{h_x}{\sqrt{1 + h_x^2}} + \frac{\partial \phi_\mu}{\partial h_x} \right)\Bigg|_{x_0} + \gamma \left.\sqrt{1 + h_x^2}\right|_{x_0} + (\gamma_{sl} - \gamma_{sg}) + \phi_\mu(h, h_x)|_{x_0} = 0. \tag{2.15}$$

Based on the derivations of Dai *et al.* (2008), we propose to decompose the vdW interactions, $\phi_\mu(h, h_x)$, into two parts: a height-dependent part, and a slope-dependent

https://doi.org/10.1017/jfm.2018.255 Published online by Cambridge University Press

part: $\phi_\mu = (\phi_{\mu,1}(h) + \phi_{\mu,2}(h)) - \phi_{\mu,2}(h)\sqrt{1+(h_x)^2}$; using the long-wave approximation, this form further simplifies to $\phi_\mu = \phi_{\mu,1}(h) - (1/2)\phi_{\mu,2}(h)(h_x)^2$; note that for parallel interfaces, $h_x = 0$, we recover the original height-dependent potential. An alternative way to arrive at the proposed form for the vdW forces is based on simple symmetry arguments: ϕ_μ cannot be linearly dependent on h_x as it should have the same sign everywhere around the droplet; therefore it must be a function of even powers of h_x, leading, in the simplest case, to the proposed gradient-squared form above.

The augmented Young equation can thus be written as

$$-h_x\left((\gamma-\phi_{\mu,2})\frac{h_x}{\sqrt{1+h_x^2}}\right)\Bigg|_{x_0} + \gamma\ \sqrt{1+h_x^2}\Bigg|_{x_0} + (\gamma_{sl}-\gamma_{sg}) + \phi_\mu(h,h_x)|_{x_0} = 0. \tag{2.16}$$

Simplifying this equation leads to the following relation: $\gamma\cos\theta_Y = [\gamma - \phi_{\mu,2}(h=0)]\cos\theta_\mu + [\phi_{\mu,1}(h=0) + \phi_{\mu,2}(h=0)]$. Combining the augmented Young equation (2.16) and the continuity constraint (2.14) leads to the following condition at the contact line:

$$\left((\gamma-\phi_{\mu,2})\frac{h_x^2}{\sqrt{1+h_x^2}}\right)\Bigg|_{x_0} = 0. \tag{2.17}$$

To satisfy this condition at the contact line, we either need to have $h_x(x_0) = 0$, leading to a zero microscopic angle as before, or $\phi_{\mu,2}(h=0) = \gamma$, which does not constrain the value of the microscopic contact angle; this allows the microscopic angle to naturally arise as part of the solution; this outcome is consistent with the predictions of non-local density functional theory (Snoeijer & Andreotti 2008). The augmented Young equation (2.16) simplifies to $\gamma\cos\theta_Y = \phi_{\mu,1}(h=0) + \gamma$; having $\phi_{\mu,1}(h=0) = \mathcal{S}$ therefore leads to the Young equation $\gamma\cos\theta_Y = \gamma_{sg} - \gamma_{sl}$.

Allowing for slope dependence of the vdW forces therefore leads to a form of the free energy that satisfies all the constraints of the partial-wetting regime. Using the long-wave approximation, i.e. $\sqrt{1+(h_x)^2} \approx 1 + (1/2)(h_x)^2$, the total Helmholtz free energy can be written as

$$\Gamma = \int_0^{x_0}\left(f(h) + \frac{1}{2}\kappa(h)(h_x)^2\right)\mathrm{d}x, \tag{2.18}$$

which, interestingly, resembles the Cahn–Hilliard formulation (Cahn & Hilliard 1958). The free energy here is divided into a bulk contribution, $f(h) = (1/2)\rho g h^2 - \mathcal{S} + \phi_{\mu,1}(h)$, and an interfacial contribution with a height-dependent interfacial tension, $\kappa(h) = \gamma - \phi_{\mu,2}(h)$. The above constraints on $\phi_{\mu,1}$ and $\phi_{\mu,2}$, therefore, lead to $f(h=0) = 0$ and $\kappa(h=0) = 0$, which allow for compactly supported droplets sitting on a dry solid substrate (Benzi *et al.* 2011; Cueto-Felgueroso & Juanes 2012; Pahlavan *et al.* 2015). Note that the height-dependent interfacial term leads to a new nonlinear term of the Kadar–Parisi–Zhang (KPZ) type (Kardar, Parisi & Zhang 1986); similar forms have also been recently proposed in the context of active suspensions (Stenhammar *et al.* 2013; Wittkowski *et al.* 2014). The idea of an order-parameter-dependent interfacial tension has been proposed in the context of binary alloys (Cahn 1961) and polymer blends (de Gennes 1980), and the dependence of surface tension on height has also been recently proposed in the context of

https://doi.org/10.1017/jfm.2018.255 Published online by Cambridge University Press

capillary waves on thin liquid films (MacDowell, Benet & Katcho 2013; MacDowell *et al.* 2014). In the context of moving contact lines, Shikhmurzaev (1997, 2007) has proposed that the idea of a dynamic surface tension close to the contact line can resolve the moving contact-line singularity and lead to a natural emergence of the dynamic contact angle (Sibley *et al.* 2015); both these features are also reproduced in our model (Pahlavan *et al.* 2015).

2.2. *Thin-film model: generalized disjoining pressure*

Having defined the free energy, we can write the evolution equation for the height of the liquid film in the form of a mass-conservative gradient flow as (Hohenberg & Halperin 1977; Cross & Hohenberg 1993; Bray 2002)

$$\frac{\partial h}{\partial t} = \frac{\partial}{\partial x}\left(\mathcal{M}\frac{\partial}{\partial x}\left(\frac{\delta \Gamma}{\delta h}\right)\right), \tag{2.19}$$

where $\mathcal{M}$ represents the mobility, and the variational derivative of the free energy is defined as $\delta\Gamma/\delta h = \partial\Gamma/\partial h - \partial/\partial x[\partial\Gamma/\partial(h_x)]$ (Anderson, McFadden & Wheeler 1998).

An alternative way to arrive at the same thin-film model is to start from the Navier–Stokes equations of motion and simplify them using the lubrication approximation:

$$\rho\left(\frac{\partial \boldsymbol{u}}{\partial t} + \boldsymbol{u}\cdot\nabla\boldsymbol{u}\right) = -\nabla P + \nabla\cdot\boldsymbol{T} - \rho g\boldsymbol{e}_z, \tag{2.20}$$

in which ρ is the liquid density, $\boldsymbol{u} = (u, w)$ is the velocity field, P is the isotropic liquid pressure, $\boldsymbol{T}$ is the stress tensor, and the last term in the equation represents the gravitational force. The stress tensor can be further decomposed into two parts, $\boldsymbol{T} = \boldsymbol{\tau} + \boldsymbol{M}$, where $\boldsymbol{\tau}$ is the deviatoric stress and $\boldsymbol{M}$ represents the stress due to external body forces, taken to be zero in this work.

We non-dimensionalize the equations in the following way: $\tilde{x} = x/L$, $\tilde{z} = z/H$, $\tilde{h} = h/H$, $\tilde{u} = u/U$, $\tilde{w} = w/(\epsilon U)$, $\tilde{t} = t/(\mu L^4/\gamma H^3)$, $\tilde{P} = P/(\gamma H/L^2)$ and $\tilde{\boldsymbol{\tau}} = \boldsymbol{\tau}/(\gamma H^2/L^3)$, where $\epsilon = H/L$, and H and L represent a characteristic height and length, respectively. This leads to three dimensionless groups, $Re = \rho UH/\mu$, $\tilde{Ca} = Ca/\epsilon^3$ with $Ca = \mu U/\gamma$, and $Bo = (L/l_\gamma)^2$, with $l_\gamma = \sqrt{\gamma/\rho g}$ as the capillary length.

The above equations of motion then need to be supplemented by boundary conditions at the wall and at the liquid–gas interface. At the wall, we impose a Navier slip boundary condition: $\tilde{u}|_{\tilde{z}=0} = \beta\partial\tilde{u}/\partial\tilde{z}|_{\tilde{z}=0}$, where $\beta = b/H$ is the non-dimensional slip or extrapolation length (Granick, Zhu & Lee 2003; Neto *et al.* 2005; Lauga, Brenner & Stone 2007); we also assume no penetration at the wall: $\tilde{w}|_{\tilde{z}=0} = 0$. At the liquid–gas interface, one must satisfy the kinematic boundary condition $\tilde{w}_s = (1/\tilde{Ca})\partial\tilde{h}/\partial\tilde{t} + \tilde{u}_s\partial\tilde{h}/\partial\tilde{x}$, where $\tilde{u}_s$ and $\tilde{w}_s$ are the velocity components at the interface. The stress boundary condition at the interface can be written as

$$([P]\boldsymbol{I} - [\boldsymbol{T}])\cdot\boldsymbol{n} = (\gamma\mathcal{K} + \Phi)\boldsymbol{n}, \tag{2.21}$$

where $[-]$ represents the jump across the interface, $\boldsymbol{n} = (-h_x, 1)/\sqrt{1+h_x^2}$ is the unit vector normal to the interface, $\boldsymbol{t} = (1, h_x)/\sqrt{1+h_x^2}$ is the unit vector tangent to the interface, $\mathcal{K} = -\nabla_s\cdot\boldsymbol{n} = h_{xx}/(1+h_x^2)^{3/2}$ represents the curvature with $\nabla_s = (\boldsymbol{I} - \boldsymbol{n}\otimes\boldsymbol{n})\cdot\nabla$. The jump in the liquid pressure and stress across the interface is represented by the

https://doi.org/10.1017/jfm.2018.255 Published online by Cambridge University Press

terms on the right-hand side of the equation: the first term gives the Laplace pressure jump due to the interface curvature, Φ arises due to the intermolecular interactions between the solid–liquid and liquid–gas interfaces and only becomes relevant when these two interfaces are closer than a few nanometres (Bonn *et al.* 2009; Israelachvili 2011).

Using the above non-dimensionalization and long-wave approximation, $\epsilon \ll 1$, and negligible inertia, $\epsilon Re \ll 1$, and surface tension-dominated flow, $\tilde{Ca} = O(1)$, the x-momentum equation reduces to $0 = -\partial\tilde{P}/\partial\tilde{x} + \partial\tilde{\tau}_{zx}/\partial\tilde{z}$. Further, assuming $\epsilon^3 Re \ll 1$, the z-momentum equation further simplifies to $0 = -Bo - \partial\tilde{P}/\partial\tilde{z}$. The slip and kinematic boundary conditions remain unchanged under the lubrication approximation. The stress boundary condition, however, simplifies further; the tangential component becomes $[\tilde{\tau}_{zx}] = 0$ and the normal component reduces to $[\tilde{P}] = -\tilde{h}_{\tilde{x}\tilde{x}} + \tilde{\Phi}$. The deviatoric stress is a function of the strain rate $\boldsymbol{\epsilon} = (\boldsymbol{\nabla u} + \boldsymbol{\nabla u}^{\mathrm{T}})/2$, and for a Newtonian liquid can be simply written as $\tau_{ij} = \mu(\partial u_i/\partial x_j + \partial u_j/\partial x_i)$. Using this definition and integrating the z-momentum equation, and then applying the normal stress boundary condition, we can write the liquid pressure as follows: $\tilde{P} = Bo(\tilde{h} - \tilde{z}) - \tilde{h}_{\tilde{x}\tilde{x}} + \tilde{\Phi}$.

Integrating the continuity equation and using the kinematic boundary condition, we arrive at $(1/\tilde{Ca})\partial\tilde{h}/\partial\tilde{t} + \partial/\partial\tilde{x}\int_0^{\tilde{h}} \tilde{u}\,\mathrm{d}\tilde{z} = 0$.

Replacing the x-velocity component in the above equation we therefore arrive at the evolution equation for the height of the film:

$$\frac{\partial\tilde{h}}{\partial\tilde{t}} = \frac{\partial}{\partial\tilde{x}}\left\{\left[\frac{\tilde{h}^3}{3} + \beta\tilde{h}^2\right]\frac{\partial\tilde{P}}{\partial\tilde{x}}\right\}. \tag{2.22}$$

Comparing (2.22) above and (2.19) in the main manuscript, it is evident that they are equivalent if $\tilde{P} = \delta\tilde{\Gamma}/\delta\tilde{h} = \mathrm{d}\tilde{f}/\mathrm{d}\tilde{h} - \sqrt{\tilde{\kappa}}(\partial/\partial\tilde{x})(\sqrt{\tilde{\kappa}}\tilde{h}_{\tilde{x}})$, where $\tilde{\Gamma} = \Gamma/(\gamma H^2/L^2)$, $\tilde{f} = f/(\gamma H^2/L^2)$, and $\tilde{\kappa} = \kappa/\gamma$; we therefore find the disjoining pressure to be

$$\tilde{\Phi}(\tilde{h}, \tilde{h}_{\tilde{x}}, \tilde{h}_{\tilde{x}\tilde{x}}) = \frac{\mathrm{d}\tilde{\phi}_{\mu,1}}{\mathrm{d}\tilde{h}} + \sqrt{\tilde{\phi}_{\mu,2}}\frac{\partial}{\partial\tilde{x}}\left(\sqrt{\tilde{\phi}_{\mu,2}}\tilde{h}_{\tilde{x}}\right), \tag{2.23}$$

where $\tilde{\phi}_{\mu,1} = \phi_{\mu,1}/(\gamma H^2/L^2)$ and $\tilde{\phi}_{\mu,2} = \phi_{\mu,2}/\gamma$, and $\tilde{\Phi}$ is a generalized disjoining pressure that depends not only on the film height, but also on its slope and curvature. Similar ideas for a generalized disjoining pressure have been proposed in the past: by integrating the intermolecular interactions in a liquid wedge, Miller & Ruckenstein (1974), Hocking (1993) and Indeikina & Chang (1999) derived a slope-dependent disjoining pressure, which was later generalized by Wu & Wong (2004), who incorporated the interactions with the molecules of the gas phase and showed that it leads to the appearance of a higher-order curvature term in the disjoining pressure. Snoeijer & Andreotti (2008) compared these results with the predictions of Keller & Merchant (1991) and Merchant & Keller (1992), and showed that the disjoining pressures do not recover the correct macroscopic Young contact angle. Dai *et al.* (2008) later showed that the form derived by Wu & Wong (2004) does not recover the classical Lifshitz formulation (Dzyaloshinskii, Lifshitz & Pitaevskii 1961) in the limit of parallel interfaces, and derived a new consistent form for the disjoining pressure. The functional form of disjoining pressure we have proposed here in (2.23) resembles that of Dai *et al.* (2008), and simplifies to a height-dependent form for parallel interfaces, recovering the classical height-dependent Lifshitz theory for parallel interfaces.

https://doi.org/10.1017/jfm.2018.255 Published online by Cambridge University Press

Information about the detailed form of the disjoining pressure becomes essential in studying many phenomena such as moving contact lines (Gogotsi *et al.* 2001; Sibley, Savva & Kalliadasis 2012; Sibley *et al.* 2015), the final stages of coalescence of drops (Yiantsios & Davis 1991; Leal 2004; Zeng *et al.* 2007; Li 2016) or in applications such as solidification (Tao, Yeckel & Derby 2016). Here, we further show the consequences of the form of the disjoining pressure on the instability and dewetting of thin liquid films in the partial-wetting regime.

3. Equilibrium solutions

Here, we review the analysis of Bertozzi, Grün & Witelski (2001), Glasner & Witelski (2003) and Gratton & Witelski (2008) for equilibrium solutions of the thin-film equation. We use the following form of the disjoining pressure for parallel interfaces, consisting of the 'non-retarded' attractive vdW interactions and a short-ranged repulsive term: $\Pi(h) = \mathrm{d}\phi_{\mu,1}/\mathrm{d}h = \mathcal{A}/(h+d_0)^3(1-(h_f+d_0)/(h+d_0))$, with $d_0 = \sqrt{\mathcal{A}/6\pi\gamma} \approx 0.2$ nm representing the Born repulsion length (Sharma 1993*a*,*b*; de Gennes *et al.* 2004; Dai *et al.* 2008; Israelachvili 2011; Pahlavan *et al.* 2015); this form of disjoining pressure is regularized to allow for the film heights to go to zero.

Here, $\mathcal{A}$ represents the Hamaker constant, and h_f represents the equilibrium or precursor film thickness. In our model, the height dependence of surface tension does allow the droplets to have a compact support without a precursor film, i.e. $h_f = 0$ (Pahlavan *et al.* 2015) (see figure 3*b*). However, for the purpose of the present study, we focus on thin films with a surrounding precursor film of non-zero height ($h_f > 0$) since we are interested in modelling dewetting and coarsening phenomena, and our objective is to compare the results of the new model with the existing results on the classical model with a constant surface tension; this regime is commonly known as pseudopartial wetting (Brochard-Wyart *et al.* 1991). We can simplify the form of the disjoining pressure by shifting the heights by d_0, i.e. $\bar{h} = h + d_0$, which leads to $\Pi(h) = \mathcal{A}/h^3(1-h_f/h)$, where we have dropped the overbars for convenience of notation. Since both components of the disjoining pressure arise from the same source (intermolecular interactions between the interfaces), we believe it is reasonable to assume they would follow the same scalings; we therefore define $\phi_{\mu,2}(h) = \gamma\phi_{\mu,1}(h)/\phi_{\mu,1}(h_f)$, leading to $\kappa(h) = \gamma(1-\phi_{\mu,1}(h)/\phi_{\mu,1}(h_f))$, thereby $\kappa(h_f) = 0$. We take $\mathcal{A} = -6h_f^2\mathcal{S}$, which leads to $\phi_{\mu,1}(h_f) = \mathcal{S}$.

With the above definition of the disjoining pressure, we can now write the bulk free energy as follows:

$$\tilde{f}(\tilde{h}) = \frac{1}{2}Bo\,\tilde{h}^2 - \frac{\delta^2}{\tilde{h}^2}\left(\frac{1}{2} - \frac{\delta}{3\tilde{h}}\right) + \frac{1}{6}, \tag{3.1}$$

where $\delta = h_f/H$ is the non-dimensional precursor film height, and we have chosen $L^2/H^2 = \gamma h_f^2/\mathcal{A} = 1/(6(1-\cos\theta_Y))$.

At equilibrium, the thin-film equation (2.19) simplifies to

$$\tilde{P} = \frac{\delta\tilde{\Gamma}}{\delta\tilde{h}} = \frac{\mathrm{d}\tilde{f}}{\mathrm{d}\tilde{h}} - \sqrt{\tilde{\kappa}}\frac{\mathrm{d}}{\mathrm{d}\tilde{x}}\left(\sqrt{\tilde{\kappa}}\frac{\mathrm{d}\tilde{h}}{\mathrm{d}\tilde{x}}\right), \tag{3.2}$$

where $\tilde{P}$ is a constant pressure; the fixed points of the above equation are the solutions of $\tilde{P} = \mathrm{d}\tilde{f}/\mathrm{d}\tilde{h}$. The typical form of the dimensionless free energy $\tilde{f}(\tilde{h})$ is shown in

https://doi.org/10.1017/jfm.2018.255 Published online by Cambridge University Press

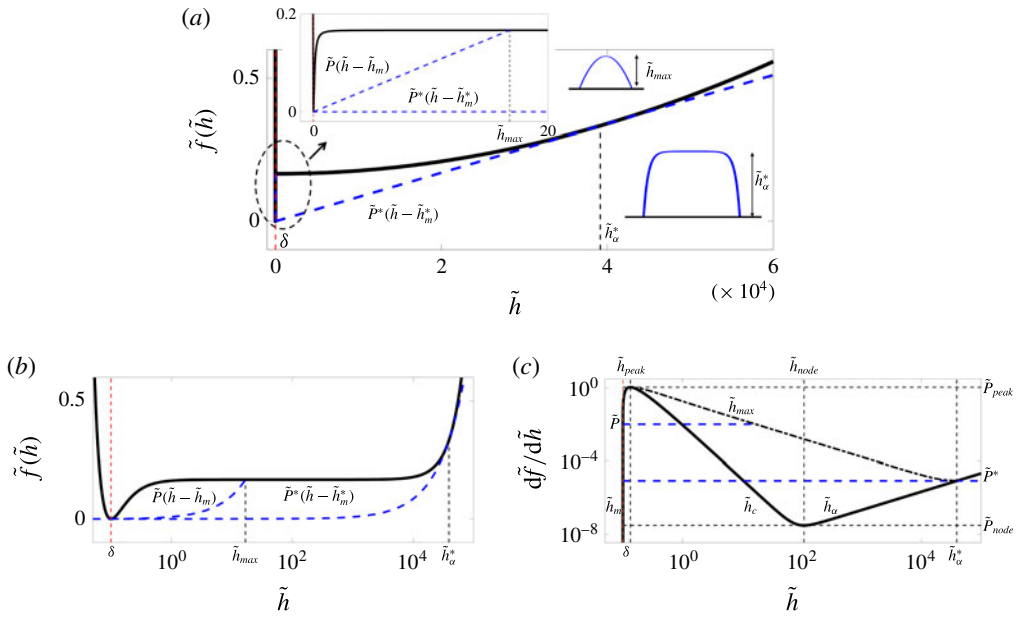


FIGURE 2. (Colour online) (*a*) The bulk free energy $\tilde{f}(\tilde{h})$ given by (3.1) with $Bo = 2.2 \times 10^{-10}$ and $\delta = 0.1$ (solid line). The blue dashed line shows the Maxwell double-tangent construction, which is tangent to the bulk free energy at $\tilde{h}_m^*$, the precursor film thickness, and at $\tilde{h}_\alpha^*$, the puddle height. The inset shows a zoomed-in view of the bulk free energy for small heights. Here, an arbitrary line with slope $\tilde{P}^* < \tilde{P} < \tilde{P}_{peak}$ is tangent to the free energy at $\tilde{h}_m$ and intersects it at $\tilde{h}_{max}$ (blue dashed line). (*b*) The bulk free energy redrawn on a semilog scale. While vdW forces act at nanoscale, gravity only becomes relevant on the millimetre scale; this 6 orders of magnitude separation of scales is shown here. Note that the tangent lines become curved in this semilog representation. (*c*) The bulk pressure defined as $\mathrm{d}\tilde{f}/\mathrm{d}\tilde{h}$. Droplet solutions exist for $\tilde{P}^* < \tilde{P} < \tilde{P}_{peak}$, where a typical constant pressure line ($\tilde{P} = \text{const.}$) intersects the curve at three fixed points corresponding to the three branches $\tilde{h}_m$, $\tilde{h}_c$ and $\tilde{h}_\alpha$, as indicated. Uniform films on the $\tilde{h}_c$ branch are linearly unstable since their corresponding $\mathrm{d}^2\tilde{f}/\mathrm{d}\tilde{h}^2 < 0$. The $\tilde{h}_{max}$ branch shows the maximum height of the droplet solutions surrounded by a corresponding film of thickness $\tilde{h}_m$; these are solutions homoclinic to $\tilde{h}_m$, where a line with slope $\tilde{P}$ is tangent to the bulk free energy at $\tilde{h}_m$ and intersects it at $\tilde{h}_{max}$ (the blue dashed tangent line). In the limit of very large drops (i.e. puddles) $\tilde{h}_m$ and $\tilde{h}_{max}$ approach $\tilde{h}_m^*$ and $\tilde{h}_\alpha^*$, respectively, and we recover the common tangent line with slope $\tilde{P}^*$ (the blue dashed tangent line) (see also Brochard-Wyart *et al.* 1991; de Gennes *et al.* 2004; Gratton & Witelski 2008).

figure 2. Within the range $\tilde{P}_{node} < \tilde{P} < \tilde{P}_{peak}$, we can find three fixed points. Using a singular perturbation analysis in the limit $\delta \to 0$, we find these points to be: $\tilde{h}_m = \delta + \delta^2 P + \delta^3(4P^2 - Bo) + O(\delta^4)$, $\tilde{h}_c = P^{-1/3}\delta^{2/3} - (1/3)\delta + 1/3(BoP^{-5/3} - 2/3P^{1/3})\delta^{4/3} + O(\delta^{5/3})$ and $\tilde{h}_\alpha = P/Bo - (Bo^2/P^3)\delta^2 + (Bo^3/P^4)\delta^3 + O(\delta^4)$, where, to leading order, only the equilibrium film thickness is independent of the pressure. The fixed points obtained here are not affected by the height dependence of the surface tension $\tilde{\kappa}(\tilde{h})$ as they only depend on the bulk free energy (Gratton & Witelski 2008). The pressure

https://doi.org/10.1017/jfm.2018.255 Published online by Cambridge University Press

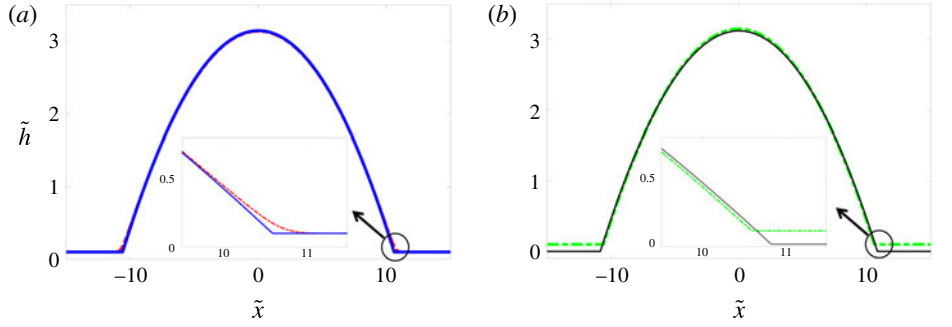


FIGURE 3. (Colour online) Equilibrium droplet profiles for (*a*) constant (red dash-dotted line) and height-dependent (solid blue line) surface tension models with a surrounding precursor film, and (*b*) the height-dependent surface tension model with (green dash-dotted line) and without (solid black line) a surrounding precursor film.

in the liquid phase, however, can be affected by the non-constant surface tension, as we will show later; this pressure change will then affect the fixed points.

The heights $\tilde{h}_m$ and $\tilde{h}_\alpha$ are saddle points, whereas $\tilde{h}_c$ is a centre (Gratton & Witelski 2008). In the range of $\tilde{P}_{node} < \tilde{P} < \tilde{P}_{peak}$, we can find three types of solutions that are bounded in height (Thiele *et al.* 2001*b*; Gratton 2008): localized hole/dimple solutions that are homoclinic to $\tilde{h}_\alpha$ in the range $\tilde{P}_{node} < \tilde{P} < \tilde{P}^*$, droplet solutions that are homoclinic to $\tilde{h}_m$ in the range $\tilde{P}^* < \tilde{P} < \tilde{P}_{peak}$, and heteroclinic orbits from $\tilde{h}_m$ to $\tilde{h}_\alpha$ at $\tilde{P} = \tilde{P}^*$. To obtain the maximum height of these droplets, we integrate (3.2) as follows:

$$\mathcal{R}(\tilde{h}) \equiv \frac{1}{2}\left(\tilde{\kappa}(\tilde{h})\left(\frac{\mathrm{d}\tilde{h}}{\mathrm{d}\tilde{x}}\right)^2\right) = \tilde{f}(\tilde{h}) - \tilde{f}(\tilde{h}_m) - \tilde{P}(\tilde{h} - \tilde{h}_m), \tag{3.3}$$

where at the maximum height of the drop we have $\mathrm{d}\tilde{h}/\mathrm{d}\tilde{x} = 0$, i.e. $\mathcal{R}(\tilde{h}_{max}) = 0$; in the limit $\delta \to 0$, we can then obtain $\tilde{h}_{max} = (1/Bo)(\tilde{P} - \sqrt{\tilde{P}^2 - Bo/3}) + (\tilde{P}/\sqrt{\tilde{P}^2 - Bo/3})\delta + O(\delta^2)$, which is the branch shown in figure 2(*c*). As the pressure decreases towards $\tilde{P}^*$, a saddle–saddle heterogeneous orbit appears between $\tilde{h}_m$ and $\tilde{h}_\alpha$, and the $\tilde{h}_{max}$ branch intersects with the $\tilde{h}_\alpha$ branch. At this point, we then obtain $\tilde{P}^* = \sqrt{Bo/3} + (Bo/2)\delta + O(\delta^2)$; this critical value of pressure is the slope of the Maxwell common tangent line (Rowlinson & Widom 2013) shown in figure 2 and satisfies the following equations:

$$\tilde{P}^* = \frac{\tilde{f}(\tilde{h}^*_\alpha) - \tilde{f}(\tilde{h}^*_m)}{\tilde{h}^*_\alpha - \tilde{h}^*_m}, \tag{3.4a}$$

$$\tilde{P}^* = \left.\frac{\mathrm{d}\tilde{f}}{\mathrm{d}\tilde{h}}\right|_{\tilde{h}^*_m} = \left.\frac{\mathrm{d}\tilde{f}}{\mathrm{d}\tilde{h}}\right|_{\tilde{h}^*_\alpha}, \tag{3.4b}$$

where $\tilde{h}^*_m$ and $\tilde{h}^*_\alpha$ are the values of $\tilde{h}_m$ and $\tilde{h}_\alpha$ as calculated at pressure $\tilde{P} = \tilde{P}^*$.

At $\tilde{P}_{node}$ and $\tilde{P}_{peak}$, the $\tilde{h}_c$ branch merges with the other two branches and we have $\mathrm{d}^2\tilde{f}/\mathrm{d}\tilde{h}^2 = 0$. Following the procedure above, in the limit of $\delta \to 0$ and

https://doi.org/10.1017/jfm.2018.255 Published online by Cambridge University Press

using a singular perturbation analysis, we find the corresponding film heights: $\tilde{h}_{peak} = (4/3)\delta + (4/3)^5(Bo/3)\delta^3 + O(\delta^7)$ and $\tilde{h}_{node} = (3/Bo)^{1/4}\delta^{1/2} - (1/3)\delta + O(\delta^2)$, which lead to the following pressures: $\tilde{P}_{peak} = (27/256\delta) + (4Bo/3)\delta + O(\delta^3)$ and $\tilde{P}_{node} = 4(Bo/3)^{3/4}\delta^{1/2} - (Bo/3)\delta - 2/3(Bo/3)^{5/4}\delta^{3/2} + O(\delta^2)$, which mark the upper and lower boundaries of the pressure range for which equilibrium droplet solutions exist. Note that the results we have obtained so far are only indirectly affected by the height dependence of surface tension through the change of liquid pressure at equilibrium, as we show later.

The droplet solutions of (3.2) can be divided into three regions: (i) core, (ii) contact line and (iii) equilibrium film. Here, we focus on the limit of small drops, where gravity can be neglected ($Bo \to 0$). In the core (region (i)), away from the contact line and in the absence of intermolecular forces, surface tension is the dominant force, and equation (3.2) simplifies to $\tilde{P} = -\tilde{h}_{\tilde{x}\tilde{x}}$, leading to a parabolic profile, $\tilde{h}_{core} = (1/2)\tilde{P}(\tilde{w}^2 - \tilde{x}^2)$, where $\tilde{w}$ is the effective width of the droplet. The maximum height of the core region at its centre $\tilde{x} = 0$ is therefore $\tilde{h}_{max} = \tilde{P}\tilde{w}^2/2$. Before, we derived the maximum height of the droplet in the presence of gravity and intermolecular forces. In the limit of zero Bond number, we can then show $\tilde{h}_{max} = 1/(6\tilde{P}) + \delta + O(\delta^2)$; equating this to the maximum height of the parabolic core, we find the effective width of the drop to leading order: $\tilde{w} = 1/(\sqrt{3}\tilde{P})$. In the second region (region (ii)), i.e. the region near the contact line, the drop profile asymptotically matches the droplet core to the equilibrium film outside. In this region, we use the following transformation $\tilde{h}(\tilde{x}) = \delta\tilde{H}(\tilde{x})$ with $\tilde{x} = -\tilde{w} + \delta\tilde{z}$, and defining $\tilde{f}(\tilde{h}) \equiv \tilde{F}(\tilde{H})$ we rescale (3.2) to leading order as follows:

$$\frac{\mathrm{d}\tilde{F}}{\mathrm{d}\tilde{H}} - \left(1 - \frac{\tilde{F}(\tilde{H})}{\tilde{F}(1)}\right)\tilde{H}_{\tilde{z}\tilde{z}} + \frac{1}{2\tilde{F}(1)}\frac{\mathrm{d}\tilde{F}}{\mathrm{d}\tilde{H}}\tilde{H}_{\tilde{z}}^2 = 0, \tag{3.5}$$

where we have used the definition $\tilde{\kappa} = 1 - \tilde{F}(\tilde{H})/\tilde{F}(1)$, which appears in the second term. This equation can be integrated to obtain $\tilde{H}_{\tilde{z}}^2/2 = -\tilde{F}(1)$, relating the slope of the profile in the contact-line region to the intermolecular forces. Consistent with the experimental observations (Pompe & Herminghaus 2000) and density functional calculations (Snoeijer & Andreotti 2008), the height dependence of surface tension leads to a non-zero contact angle at the contact line. In this model the droplet width is a finite value that can be unambiguously defined, where the droplet meets the surrounding wet or dry surface at a non-zero angle (figure 3*b*). This is in clear contrast with the classical model with a constant surface tension, $\tilde{\kappa} = 1$, for which we obtain $\tilde{H}_{\tilde{z}}^2/2 = \tilde{F}(\tilde{H}) - \tilde{F}(1)$, leading to a zero contact angle as the droplet asymptotically meets the precursor film, i.e. $\tilde{H} \to 1$ (figure 3*a*). In the classical model, only the macroscopic contact angle far away from the contact line can be non-zero; we therefore need to take the limit of $\tilde{H} \to \infty$, where $\tilde{F}(\tilde{H}) \to 0$, recovering the result $\tilde{H}_{\tilde{z}}^2/2 = -\tilde{F}(1)$. Using the dimensional version of this result leads to $h_x^2/2 = \mathcal{A}/(6\gamma h_f^2)$, which simplifies to $h_x^2/2 = (1 - \cos\theta_Y)$ using the definition $\mathcal{A} = -6h_f^2\mathcal{S}$; in the limit of small contact angles ($\theta_Y \ll 1$), we can therefore relate the droplet slope to the Young contact angle: $h_x \approx \theta_Y$.

Figure 4 shows the variation of some of the droplet features as a function of its equilibrium pressure (or size) for both the classical model (with constant surface tension) and our model (with a height-dependent surface tension). The first observation is that the difference between the two models is most pronounced for very small

https://doi.org/10.1017/jfm.2018.255 Published online by Cambridge University Press

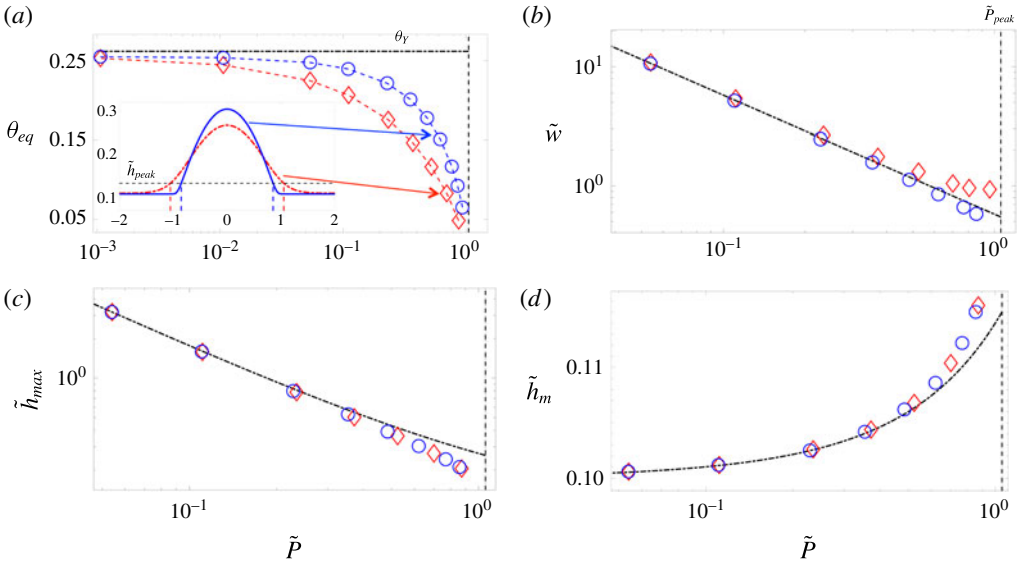


FIGURE 4. (Colour online) The variation of equilibrium droplet features with the liquid pressure in the droplet. The symbols show the result of numerical simulations with a constant surface tension (red diamonds), and a height-dependent surface tension (blue circles). The dash-dotted lines represent the theoretical predictions for small droplets, and the vertical dashed lines correspond to the $\tilde{P}_{peak}$ beyond which no droplet solutions exist. (*a*) The equilibrium contact angle defined at the inflection point of the droplet profile; the dash-dotted line represents the Young contact angle. The inset shows two typical droplet profiles of equal mass (but different equilibrium pressure, with the new model leading to smaller liquid pressures) for the constant surface tension (red dash-dotted line) and height-dependent surface tension (blue solid line) models. (*b*) Droplet width defined as the distance from centre of the drop to its edge at $\tilde{h}_{peak}$. The dash-dotted line represents $\tilde{w} = 1/(\sqrt{3}\tilde{P})$. In the constant surface tension case, the droplet core asymptotically meets the equilibrium film, leading to a larger effective width. (*c*) Maximum droplet height. The dash-dotted line represents $\tilde{h}_{max} = 1/(6\tilde{P}) + \delta + O(\delta^2)$. The height dependence of surface tension results in lower equilibrium pressures, which in turn lead to larger $\tilde{h}_{max}$ values in the small droplets. (*d*) Equilibrium film thickness. The dash-dotted line represents $\tilde{h}_m = \delta + \delta^2 P + \delta^3(4P^2 - Bo)$.

droplets, where their entire profile is influenced by the intermolecular forces; as the droplets become larger, intermolecular forces can only be felt very close to the contact line, and the difference between the two models is limited to the vicinity of this region and less relevant to macroscopic features such as width, maximum height, or even equilibrium film thickness, which is now determined by balancing the Laplace pressure due to the curvature of the core region of the drops. The equilibrium contact angle also becomes size-dependent for very small droplets (figure 4*a*), where the entire droplet geometry is influenced by the intermolecular forces; this dependence, however, is not due to the line tension effect, which would be relevant for axisymmetric drops (Amirfazli & Neumann 2004; Schimmele, Napiorkowski & Dietrich 2007; Weijs *et al.* 2011; Giro *et al.* 2017). The second observation is that for small droplets, the height-dependent surface tension model always leads to more localized profiles with larger contact angle and smaller effective width; for equal droplet mass, the height

https://doi.org/10.1017/jfm.2018.255 Published online by Cambridge University Press

dependence of surface tension leads to a lower equilibrium pressure, which according to the tangent construction shown in figure 2 leads to a larger maximum height ($\tilde{h}_{max}$) and smaller equilibrium film thickness ($\tilde{h}_m$).

All the simulations in this paper are performed assuming an equilibrium film thickness of $h_f = 1$ nm, and characteristic height $H = 10$ nm, which is the typical range of dominance of vdW forces, leading to a non-dimensional equilibrium film height of $\delta = h_f/H = 0.1$, and $Bo = (L/l_\gamma)^2 = 2.2 \times 10^{-10}$, i.e. negligible gravity (capillary length $l_\gamma = 1.5$ mm); while the influence of gravity in thin films is in principle insignificant, ignoring its role can lead to unphysical predictions (Thiele *et al.* 2001*b*).

4. Stability of uniform films

Here, we analyse the stability of uniform film solutions of (3.2) to infinitesimal and finite perturbations. Consider a uniform film of thickness $\tilde{h}_0$ that is perturbed infinitesimally by a superposition of Fourier modes as $\tilde{h} = \tilde{h}_0 + \epsilon \exp(\beta\tilde{t} + \mathrm{i}q\tilde{x})$, where β is the growth rate of the instability, $q = 2\pi/\lambda$ is the wavenumber, and $\epsilon \ll 1$. Substituting this decomposition into (2.19) and linearizing it to $O(\epsilon)$, we find

$$\beta = \tilde{h}_0^3 q^2 (q_0 - \tilde{\kappa}(\tilde{h}_0) q^2), \tag{4.1}$$

where $q_0 = -\mathrm{d}^2\tilde{f}/\mathrm{d}\tilde{h}^2|_{\tilde{h}_0}$. A uniform film becomes unstable if the growth rate is positive $\beta > 0$, or $q_0 > \tilde{\kappa}(\tilde{h}_0) q^2$. This implies that wavenumbers $q < \sqrt{q_0/\tilde{\kappa}(\tilde{h}_0)}$, or equivalently wavelengths $\lambda > \lambda_c = 2\pi\sqrt{\tilde{\kappa}(\tilde{h}_0)/q_0}$, will be unstable; surface tension damps the shorter-wavelength deformations. The curve $q_0 = 0$ separates the linearly stable and unstable regions, as shown in figure 5; the instability phase diagram can be represented in the phase space of the initial uniform film thickness $\tilde{h}_0$ versus the equilibrium film thickness $\delta = h_f/H$ (Diez & Kondic 2007) or $\tilde{h}_0$ versus Bo (Thiele *et al.* 2001*b*). The curve $q_0 = 0$ represents the boundary of the spinodal region in the free energy, where the second derivative of the bulk free energy becomes negative, $\mathrm{d}^2\tilde{f}/\mathrm{d}\tilde{h}^2|_{\tilde{h}_0} < 0$. This region is bounded by the heights $\tilde{h}_{peak}$ and $\tilde{h}_{node}$, as shown in figure 2. The region between these heights and the film heights corresponding to the tangent construction is called the binodal region, where the uniform wetted liquid films are not linearly unstable, but they can be nonlinearly unstable, i.e. if perturbed by a sufficiently large finite-amplitude perturbation they can evolve to find a lower energy state. The boundaries of the binodal region are set by $\tilde{h}_m^*$ and $\tilde{h}_\alpha^*$, as shown in figure 2. The lower and upper branches all meet at a critical point, where the bulk free energy transitions from a double-well to a single-well structure; at the critical point, we have $\mathrm{d}^2\tilde{f}/\mathrm{d}\tilde{h}^2 = 0$, and $\mathrm{d}^3\tilde{f}/\mathrm{d}\tilde{h}^3 = 0$, leading to $\tilde{h} = (5/3)\delta$, $\delta_{cr} \approx 1.9 \times 10^4$, and $Bo_{cr} \approx 7.85$. To find the fastest-growing mode, we take $\mathrm{d}\beta/\mathrm{d}q = 0$, which leads to the following expressions for the most unstable wavelength

$$\lambda_m = \sqrt{2}\lambda_c = 2\pi\sqrt{\frac{2\tilde{\kappa}(\tilde{h}_0)}{-\mathrm{d}^2\tilde{f}/\mathrm{d}\tilde{h}^2|_{\tilde{h}_0}}}, \tag{4.2}$$

and its corresponding maximum growth rate

$$\beta_m = \frac{\tilde{h}_0^3}{4\tilde{\kappa}(\tilde{h}_0)} \left(\left. \frac{\mathrm{d}^2\tilde{f}}{\mathrm{d}\tilde{h}^2} \right|_{\tilde{h}_0} \right)^2. \tag{4.3}$$

https://doi.org/10.1017/jfm.2018.255 Published online by Cambridge University Press

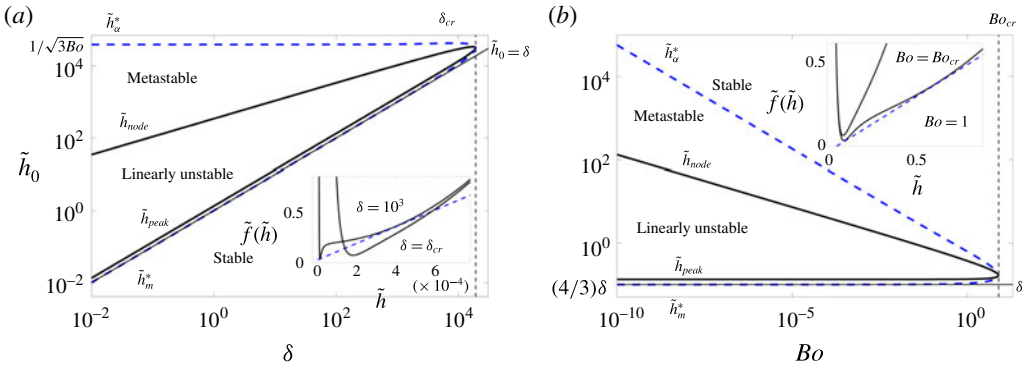


FIGURE 5. (Colour online) Stability phase diagram showing the regions where the uniform film is linearly unstable, metastable (nonlinearly unstable), and absolutely stable. (*a*) Shows the phase diagram as a function of the initial film height, $\tilde{h}_0 = h_0/H$, and the equilibrium film thickness, $\delta = h_f/H$. The full black solid line represents the marginal stability curve, where the instability growth rate, β is zero (i.e. $q_0 = -\mathrm{d}^2\tilde{f}/\mathrm{d}\tilde{h}^2|_{\tilde{h}_0} = 0$); inside the curve, the film is linearly unstable to infinitesimal perturbations, whereas outside it is linearly stable; the lower branch of the marginal stability curve is coincident with $\tilde{h}_{peak}$, whereas the upper branch represents $\tilde{h}_{node}$. The blue dashed line represents the curve of absolute stability; outside this curve, all films are absolutely stable, whereas inside it uniform films can become unstable due to finite perturbations, i.e. they are nonlinearly unstable. The upper and lower branches of the absolute stability curve represent the $\tilde{h}^*_\alpha$ and $\tilde{h}^*_m$ lines; these are the points tangent to the Maxwell double-tangent construction. In other words, while the curve of marginal stability represents the spinodal region, where $\mathrm{d}^2\tilde{f}/\mathrm{d}\tilde{h}^2|_{\tilde{h}_0} \leqslant 0$, the curve of absolute stability represents the binodal or coexistence curve. The upper and lower branches meet at the critical point, where we have $\mathrm{d}^2\tilde{f}/\mathrm{d}\tilde{h}^2 = 0$, and $\mathrm{d}^3\tilde{f}/\mathrm{d}\tilde{h}^3 = 0$, leading to $\tilde{h} = (5/3)\delta$ and $\delta_{cr} \approx 1.9 \times 10^4$, where (as shown in the inset) a transition from a double-well to a single-well structure occurs in the free energy. The dashed blue line in the inset represents the tangent construction. (*b*) Shows the phase diagram as a function of the initial film thickness, $\tilde{h}_0$, and the Bond number Bo. The same transition from a double-well to a single-well structure is observed at a critical Bond number of $Bo_{cr} \approx 7.85$ where the upper and lower branches of the stability curves meet.

We observe that both the instability wavelength and growth rate are affected by the height dependence of the surface tension. We can denote the corresponding predictions of the classical model by $\lambda_{m,\kappa c} = 2\pi\sqrt{1/q_0}$ and $\beta_{m,\kappa c} = (\tilde{h}_0^3/4)q_0^2$, where the subscript κc represents constant surface tension. The new model therefore predicts a smaller instability wavelength, $\lambda_m/\lambda_{m,\kappa c} = \sqrt{\tilde{\kappa}(\tilde{h}_0)} \leqslant 1$, and a faster growth rate $\beta_m/\beta_{m,\kappa c} = 1/\tilde{\kappa}(\tilde{h}_0) \geqslant 1$, as shown in figure 6. For very large initial thicknesses, the effect of height dependence of surface tension becomes insignificant and both models predict the same scaling for the maximum growth rate $\beta_m \sim \tilde{h}_0^{-5}$ (figure 6*b*), showing that it drastically reduces as the film thickness increases. The height dependence of surface tension, however, leads to a larger growth rate for small film thicknesses, predicting that the instability grows faster. The largest β_m corresponds to $\tilde{h}_0 = (28/15)\delta$ for the classical model and $\tilde{h}_0 \approx 1.7\delta$ for the new model. Both models predict a similar scaling for the most unstable wavelength at large thicknesses $\lambda_m \sim \tilde{h}_0^2$ (figure 6*c*), whereas for

https://doi.org/10.1017/jfm.2018.255 Published online by Cambridge University Press

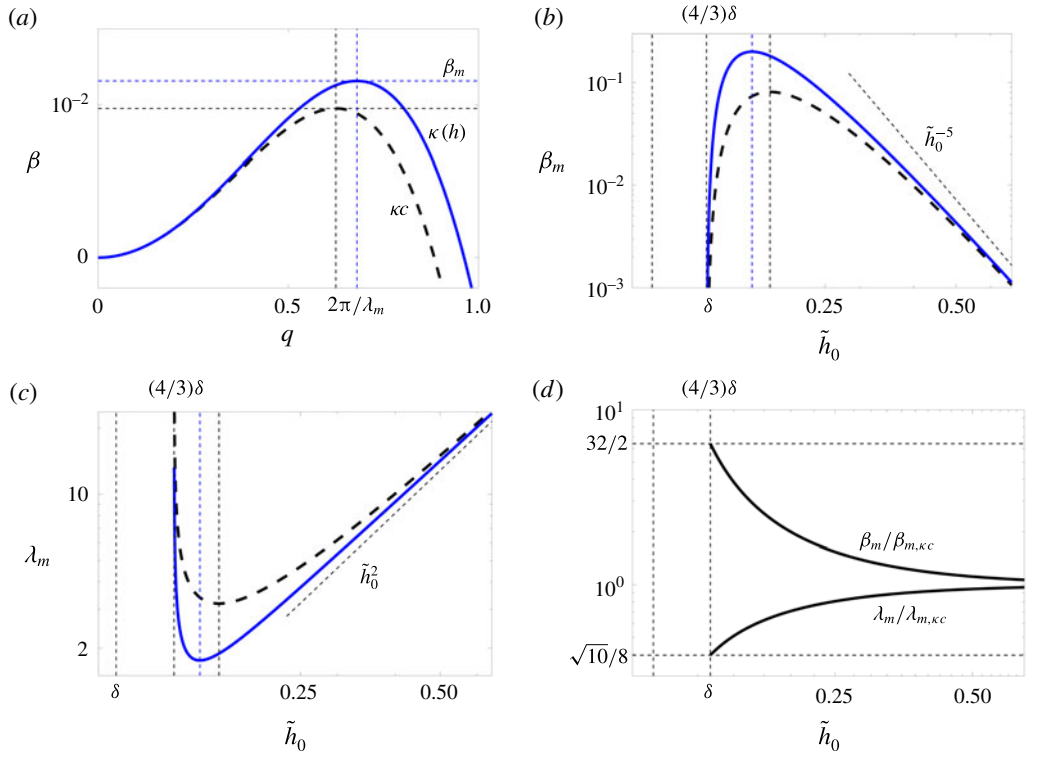


FIGURE 6. (Colour online) Linear stability analysis results. (*a*) Dispersion curve showing the instability growth rate β versus the wavenumber q for a film of thickness $\tilde{h}_0 = 4\delta$. All curves labelled with κc and $\kappa(h)$ represent the classical model with a constant surface tension and the new model with a height-dependent surface tension, respectively. The new model results in a shift to larger values for both the maximum growth rate β_m and its corresponding wavenumber, leading to a smaller wavelength of instability λ_m. (*b*) Scaling of the maximum growth rate with the thickness of the initial uniform film $\tilde{h}_0$. The vertical dashed line $(4/3)\delta$ represents the lower limit of linear instability. (*c*) Wavelength of the instability corresponding to the most unstable mode. (*d*) Ratio of predicted growth rate and instability wavelength between the new model and the classical model. It is apparent that the maximum ratio corresponds to the smallest film thickness $\tilde{h}_0 = (4/3)\delta$ where the film is linearly unstable; below the height of $\tilde{h}_0 = (4/3)\delta$ the film becomes linearly stable and the surface tension keeps decreasing until it reaches a value of zero for $\tilde{h}_0 = \delta$.

smaller heights, where the effect of variability of surface tension becomes relevant, the new model predicts smaller wavelengths. The minimum λ_m corresponds to $\tilde{h}_0 = (5/3)\delta$ for the classical model and $\tilde{h}_0 \approx 1.52\delta$ for the new model. Note that these heights are different from those concerning the maximum growth rate β_m. Further, the instability wavelength shows a much weaker dependence on the film thickness than the growth rate ($\tilde{h}_0^2$ versus $\tilde{h}_0^{-5}$). Within the linearly unstable region, the new model predicts the instability can grow up to six times faster than the predictions of the classical model (figure 6*d*) while its corresponding instability wavelength can be less than half of that in the classical model; the growth rate is therefore a more sensitive measure of the height dependence of surface tension.

https://doi.org/10.1017/jfm.2018.255 Published online by Cambridge University Press

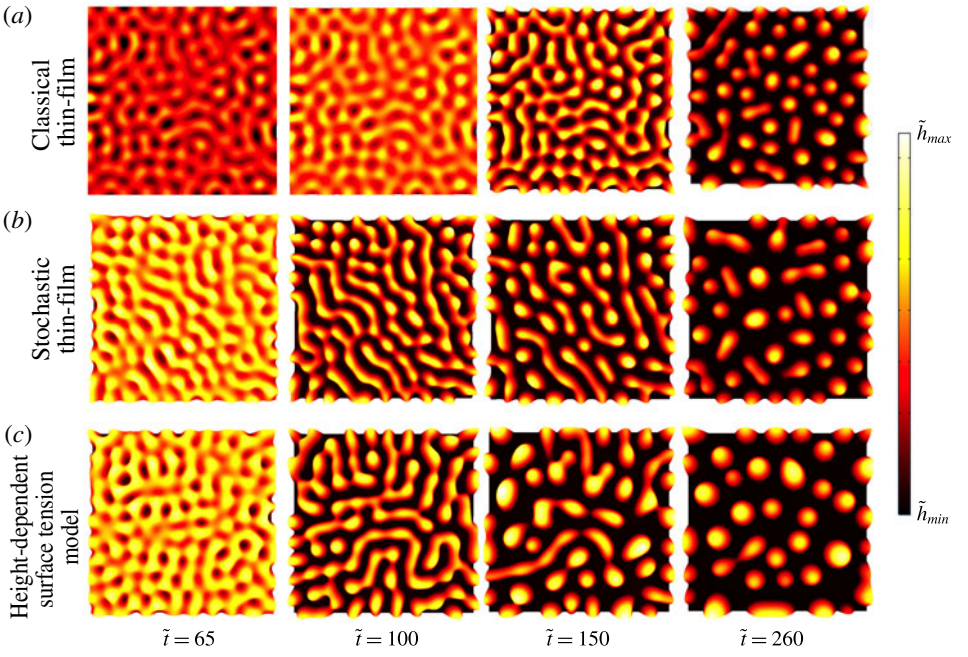


FIGURE 7. (Colour online) 2D simulations of dewetting in the spinodal regime with $\tilde{h}_0 = 2\delta$ in a domain of size $10\lambda_m$ by $10\lambda_m$; 2D profiles of $\tilde{h}(\tilde{x}, \tilde{y})$ with contour levels between $\tilde{h}_{min}$ and $\tilde{h}_{max}$ as specified are shown. (*a*) The classical thin-film equation ($\tilde{h}_{min} = 1.99\delta$, 1.86δ, δ, δ, and $\tilde{h}_{max} = 2.02\delta$, 2.16δ, 4δ, 6.7δ, respectively). (*b*) The stochastic thin-film equation (5.2) with constant surface tension at temperature $T = 50\,^{\circ}\mathrm{C}$, i.e. $\sigma = 0.039$ ($\tilde{h}_{min} = \delta$, and $\tilde{h}_{max} = 2.8\delta$, 4.3δ, 5.1δ, 7.5δ, respectively). (*c*) The new model with height-dependent surface tension ($\tilde{h}_{min} = \delta$, and $\tilde{h}_{max} = 2.8\delta$, 4.3δ, 5.1δ, 7.5δ, respectively). Both thermal fluctuations and height dependence of surface tension lead to a faster dewetting process, bringing the theoretical predictions closer to the experimental observations (Becker *et al.* 2003).

To go beyond the linear stability analysis, we conducted two-dimensional (2D) numerical simulations in the spinodal regime to examine the dewetting rate and morphologies obtained. Figure 7 shows that thermal fluctuations (see equation (5.2)) and height dependence of surface tension both lead to a faster initial dewetting. Figure 8 shows the growth of perturbations in the nonlinear simulations of dewetting using the different models. The linear stability analysis for this film thickness predicts that the growth rate of the height-dependent surface tension model is twice as fast as the classical model ($\beta_m/\beta_{m,\kappa c} = 2$). From the nonlinear simulations we find that the new model leads to a film rupture at $\tilde{t}_{r1} \approx 75$, whereas the classical model leads to a rupture time of $\tilde{t}_{r3} \approx 150$, which is in agreement with the linear stability predictions. Thermal fluctuations at $T = 50\,^{\circ}\mathrm{C}$, i.e. $\sigma = 0.039$ (see equation (5.2)), lead to a rupture around $\tilde{t}_{r2} \approx 125$, which is faster than the classical model. Figure 9 shows a more quantitative comparison of the rupture times between the classical model and the other models. The speed up observed due to the thermal noise is independent of the initial height of the film, whereas the height dependence of surface tension in the new model leads to increasingly faster rupture as the initial film height decreases. The prediction of a faster growth rate in our model deserves special attention. Earlier

https://doi.org/10.1017/jfm.2018.255 Published online by Cambridge University Press

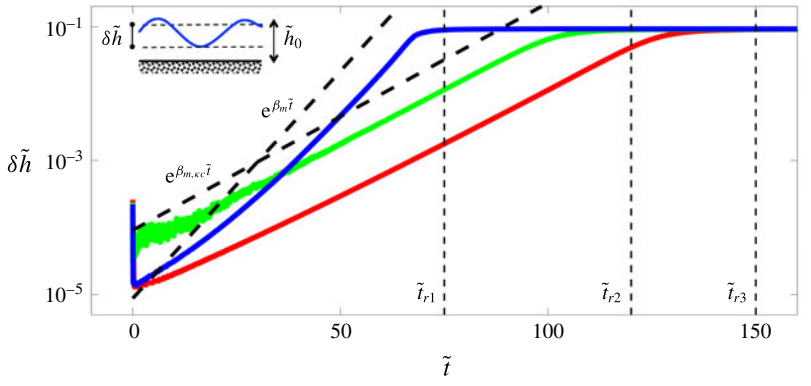


FIGURE 8. (Colour online) The growth of perturbations in the spinodal regime ($\tilde{h}_0 = 2\delta$ as in figure 7) for the classical model (solid red line), stochastic model (solid green line), and height-dependent surface tension model (solid blue line) as obtained from the nonlinear simulations. The imposed perturbations become damped at early times due to the surface tension, but then start to grow exponentially (as shown by the dashed lines).

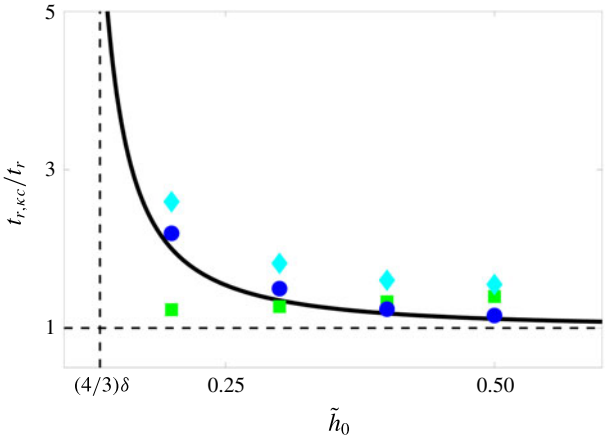


FIGURE 9. (Colour online) The ratio of the rupture times between the classical model ($t_{r,\kappa c}$) and the classical model with thermal noise (green squares), the height-dependent surface tension model without noise (blue circles) and the height-dependent surface tension model with noise (cyan diamonds). Both the thermal noise and height dependence of surface tension lead to a faster rupture time compared to the classical model. While the effect of noise is almost independent of the initial film thickness (green squares), the height dependence of surface tension leads to an increasingly faster ruptures as the film thickness decreases (blue circles). This effect becomes even more amplified when thermal noise is added to the new model (cyan diamonds). The solid line represents the ratio of the growth rates between the classical and new model as predicted from the linear stability analysis (see figure 6*d*).

studies have pointed to temporal inconsistencies between theoretical predictions and experimental observations (Becker *et al.* 2003), with experiments showing a faster initial dewetting process by more than a factor of two compared to the theoretical predictions. Our new model therefore brings theoretical predictions closer to the

https://doi.org/10.1017/jfm.2018.255 Published online by Cambridge University Press

earlier experimental observations. Our results in figure 9 further suggest that to disentangle the roles played by the height dependence of surface tension and the thermal noise, experiments with different initial heights need to be conducted.

5. Coarsening: self-similar intermediate asymptotics

5.1. *Coarsening phase diagram*

The drops formed after the dewetting process are in a metastable state; they can still communicate through the ultrathin films connecting them and thus coarsen in time to lower the overall energy of the system. Multiplying both sides of (2.19) by $\delta\Gamma/\delta\tilde{h}$, integrating in space and using the no-flux boundary conditions, we can easily show (see also Thiele *et al.* (2001*b*), Glasner & Witelski (2003)):

$$\frac{\mathrm{d}\Gamma}{\mathrm{d}\tilde{t}} = -\int \mathcal{M}\left(\frac{\partial}{\partial\tilde{x}}\left(\frac{\delta\Gamma}{\delta\tilde{h}}\right)\right)^2 \mathrm{d}\tilde{x} \leqslant 0, \tag{5.1}$$

demonstrating that the evolution governed by the thin-film equation leads to a decreasing free energy and, therefore, a thermodynamically admissible system.

Figure 10 shows space–time diagrams of the dewetting of thin liquid films of different thickness and their coarsening over time. The simulations presented here are conducted on a large domain of size $100\lambda_m$ and the frames shown are a zoomed-in view of a window of size $40\lambda_m$; these simulations show the results corresponding to the classical model with a constant surface tension; the results of the height-dependent surface tension model are very similar. In all cases we start with a uniform film of thickness $\tilde{h}_0$ on which random perturbations of amplitude $10^{-4}\tilde{h}_0$ are imposed. While all the initial thicknesses are within the linearly unstable regime (see figure 5), they lead to entirely different morphologies.

For small initial film height of $\tilde{h}_0 = 4\delta$, we observe the characteristics of the spinodal dewetting, a term originally coined by Mitlin (1993) due to its similarity to the spinodal decomposition in binary mixtures (Cahn 1961). In this regime, the distance between the drops is the same as the most unstable wavelength, i.e. we get $\approx$100 drops in a domain of size $100\lambda_m$ (Diez & Kondic 2007). The coarsening here proceeds through Ostwald ripening (Ostwald 1897), or collapse of smaller drops at the expense of growth of larger ones (Glasner & Witelski 2003).

As the initial film height increases to $\tilde{h}_0 = 10\delta$, we can immediately see in figure 10(*b*) that the number of drops formed upon dewetting and their spacing no longer follows the predictions of the linear stability analysis, i.e. fewer drops form and their spacing becomes random. This behaviour has signatures of nucleation dewetting within the linearly unstable regime (Thiele, Velarde & Neuffer 2001*a*; Thiele *et al.* 2001*b*; Diez & Kondic 2007) and shows a mixed-mode instability, i.e. a behaviour in between spinodal and nucleation regimes. Such a transition has also been reported in phase separation dynamics within the Cahn–Hilliard framework (Novick-Cohen 1985). Figure 11 shows corresponding 2D simulations of dewetting in this regime; in contrast with the spinodal regime, where holes appear around the same time with a uniform spacing, here the nucleation process begins with formation of a hole, which then laterally expands and forms a rim behind it (Seemann, Herminghaus & Jacobs 2001*b*; Fetzer *et al.* 2005; Seemann *et al.* 2005; Bäumchen & Jacobs 2010; Bäumchen *et al.* 2014). In this mixed-mode regime, the growth rate is still large enough that shortly after growth of a hole, the depression behind the dewetting rim can lead to rupture; this behaviour leads to the satellite-hole formation observed in

https://doi.org/10.1017/jfm.2018.255 Published online by Cambridge University Press

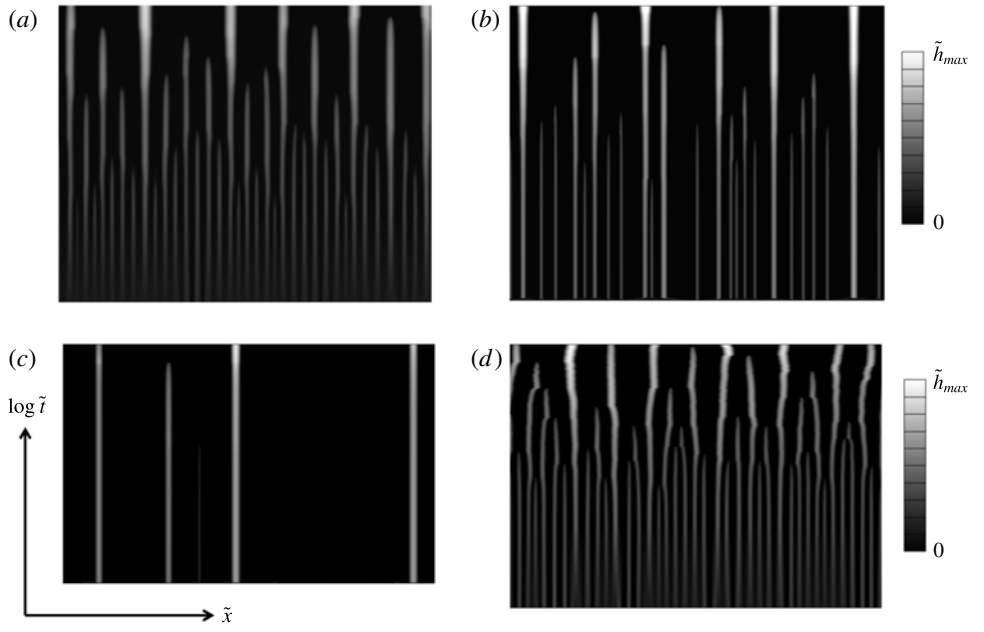


FIGURE 10. Space–time diagrams showing the evolution of drop height of the classical thin-film equation (constant surface tension); the results of the height-dependent case are similar. The simulations are done in a domain of size $100\lambda_m$ and the frames shown here show a zoom-in of a size $40\lambda_m$. In all the cases, a line coming to an end indicates an Ostwald-ripening event, in which a smaller drop feeds into larger neighbouring drops through the ultrathin film that connects them. (*a*) $\tilde{h}_0 = 4\delta$, representing the classical spinodal regime, where the number of drops is approximately set by the most unstable wavelength λ_m ($\tilde{h}_{max} = 35\delta$). (*b*) $\tilde{h}_0 = 10\delta$ representing a mixed-mode instability regime in between spinodal and nucleation regimes; here, fewer drops than the spinodal regime form and the distance between the formed drops seems to be random ($\tilde{h}_{max} = 100\delta$). (*c*) $\tilde{h}_0 = 25\delta$, which is deep into the nucleation regime, showing the formation of very few drops ($\tilde{h}_{max} = 700\delta$). (*d*) $\tilde{h}_0 = 4\delta$ and including thermal fluctuations ($T = 50\,^{\circ}\mathrm{C}$, i.e. $\sigma = 0.039$) ($\tilde{h}_{max} = 25\delta$); thermal noise enhances the lateral motion of the drops; the coarsening mechanism, however, still seems to be dominated by Ostwald ripening.

the experiments (Becker *et al.* 2003; Neto *et al.* 2003) and in the 2D simulations of figure 11. Figure 12 illustrates this nucleation process in a space–time diagram of a one-dimensional (1D) simulation of the height-dependent surface tension model with $\tilde{h}_0 = 10\delta$.

As we keep increasing the initial film thickness further to $\tilde{h}_0 = 25\delta$ (figure 10*c*), we move deeper into the nucleation regime, where fewer drops form; in this case five drops formed in random locations in a domain of size $40\lambda_m$. In the nucleation regime two time scales compete: the time scale associated with the growth of linearly unstable modes and the time scale associated with the dewetting front (Thiele *et al.* 2001*a*; Diez & Kondic 2007; Snoeijer & Eggers 2010). As we showed before, the growth rate of the most unstable mode β_m scales as $\tilde{h}_0^{-5}$, leading to significant decreases in the growth rate for thicker films, thereby favouring growth via nucleation.

https://doi.org/10.1017/jfm.2018.255 Published online by Cambridge University Press

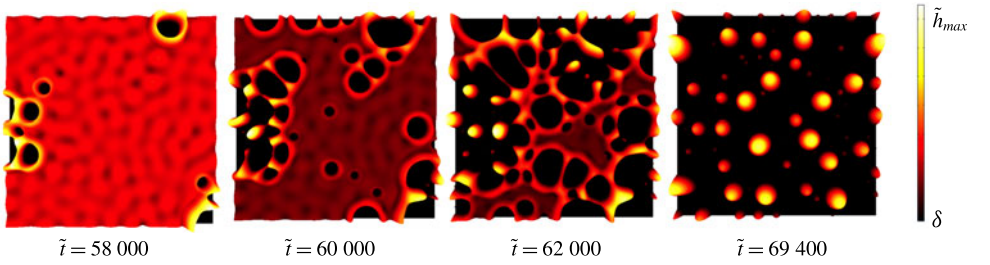


FIGURE 11. (Colour online) Nucleation dewetting for $\tilde{h}_0 = 10\delta$ for the constant surface tension model. In this regime, holes randomly appear and start expanding laterally, forming a growing rim behind them ($\tilde{h}_{max} = 30\delta$, 54δ, 70δ, 120δ, respectively). The depression behind the dewetting rim leads to the formation of satellite holes. The dewetting rims subsequently become unstable and lead to fingering and pinch off to form droplets (see Reiter & Sharma (2001), Bäumchen *et al.* (2014) for experimental details).

Since the dynamics of the coarsening process is slaved to the flux through the ultrathin equilibrium films ($\tilde{h}_m \approx \delta$) connecting the drops and the mobility scales as $\tilde{h}^3$, the coarsening dynamics are extremely slow. Two time scales are involved in this process: a fast time scale over which individual coarsening events happen, and a slow time scale between the individual events (Glasner & Witelski 2003). A full numerical simulation of the thin-film equation therefore can be computationally very expensive. Glasner & Witelski (2003) used the separation of time scales in this problem to reduce the governing partial differential equation, equation (2.19), to a system of ordinary differential equations for the droplet pressures and locations. Coarsening can proceed via two general mechanisms: coalescence of droplets or Ostwald ripening (Glasner & Witelski 2005). Their mathematical model allowed them to simulate the coarsening of a very large number ($O(10^5)$) of drops. They observed a scaling of $N \sim \tilde{t}^{-2/5}$ for the number of drops in time and also observed a transition from Ostwald-ripening-dominated (capillary-driven drainage and collapse) coarsening to coalescence-dominated coarsening as they increased the total mass of liquid in the domain.

In contrast with the findings of Glasner & Witelski (2005), we do not observe such a transition from Ostwald-ripening-dominated to coalescence-dominated coarsening (figure 10). The change in the instability mode from spinodal to nucleation leads to the formation of fewer drops as the total mass of the liquid in the domain increases, i.e. as the initial film height increases: the large distance between the drops favours coarsening through Ostwald ripening rather than coalescence. The reason Glasner & Witelski (2005) observe such a transition is that they keep the number of drops within a given domain fixed as they increase their mass; this naturally leads to wider drops that progressively get closer to each other, therefore favouring coalescence.

5.2. *Influence of thermal fluctuations*

Some experiments on thin-film dewetting (Limary & Green 2002, 2003) and nanoparticle growth in thin films (Meli & Green 2008; Woehl *et al.* 2014) have reported a crossover from diffusion-dominated to coalescence-dominated behaviour. A potential source of this transition could be thermal noise, which may play a dominant role in thin-film systems (Mecke & Rauscher 2005; Grün *et al.* 2006;

https://doi.org/10.1017/jfm.2018.255 Published online by Cambridge University Press

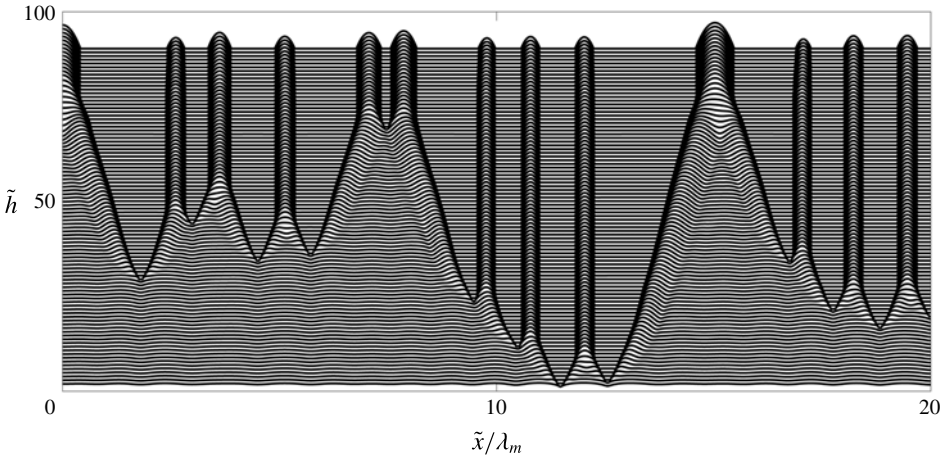


FIGURE 12. Space–time diagram of the nucleation process in the height-dependent surface tension model with $\tilde{h}_0 = 10\delta$ in a domain of size $20\lambda_m$ (each snapshot is shifted up by $10\delta = 1$). The lateral expansion of holes, growth of the rim behind the hole, and the subsequent instability of the dip behind a growing rim can all be seen in this illustration.

Fetzer *et al.* 2007*b*; Willis & Freund 2009; Belardinelli *et al.* 2016; Diez, González & Fernández 2016). To explore this possibility, we generalize the thin-film equation (2.19) by incorporating thermal noise:

$$\frac{\partial \tilde{h}}{\partial \tilde{t}} = \frac{\partial}{\partial \tilde{x}}\left(\tilde{h}^3 \frac{\partial \tilde{P}}{\partial \tilde{x}}\right) + \sigma \frac{\partial}{\partial \tilde{x}}(\tilde{h}^{3/2}\tilde{\xi}(\tilde{x}, \tilde{t})), \tag{5.2}$$

in which $\tilde{P} = \mathrm{d}\tilde{f}/\mathrm{d}\tilde{h} - \sqrt{\tilde{\kappa}}\partial/\partial\tilde{x}(\sqrt{\tilde{\kappa}}\partial\tilde{h}/\partial\tilde{x})$, with $\tilde{\kappa} = \kappa/\gamma$ and $\tilde{f} = f/(\gamma H^2/L^2)$, where H and L are characteristic height and length scales. The second term on the right-hand side of the equation represents the thermal fluctuations (Davidovitch, Moro & Stone 2005; Mecke & Rauscher 2005; Grün *et al.* 2006) with $\sigma = \sqrt{k_B T/\gamma H^2}$, where k_B is Boltzmann's constant, T represents absolute temperature and $\tilde{\xi}$ represents a spatiotemporal Gaussian white noise: $\langle\tilde{\xi}\rangle = 0$ and $\langle\tilde{\xi}(\tilde{x}, \tilde{t})\tilde{\xi}(\tilde{x}', \tilde{t}')\rangle = \delta(\tilde{x} - \tilde{x}')\delta(\tilde{t} - \tilde{t}')$ with δ as the Dirac delta function and $\langle.\rangle$ implying ensemble average over realizations of the noise.

Introducing thermal noise to the system leads to enhanced lateral motion of the drops, as seen in figure 10(*d*), and this can promote coalescence. Our simulations for the stochastic thin-film equation (5.2) within the spinodal regime, however, show the dominance of Ostwald ripening despite the enhanced lateral motion of the drops. The crossover from the diffusion-dominated to coalescence-dominated behaviour observed in the experiments (Limary & Green 2002, 2003) therefore could be a consequence of the dimensionality of the problem, i.e. 2D in the experiments versus 1D in the simulations shown in figure 10. In two dimensions, each drop can be surrounded and interact with multiple other drops, whereas in one dimension each drop only interacts with its two neighbours. To investigate this, we have conducted 2D nonlinear simulations, which point to the dominance of coalescence events at short times and Ostwald ripening at long times, as shown in figure 13, which corresponds to the height-dependent surface tension model; similar results are obtained for both

https://doi.org/10.1017/jfm.2018.255 Published online by Cambridge University Press

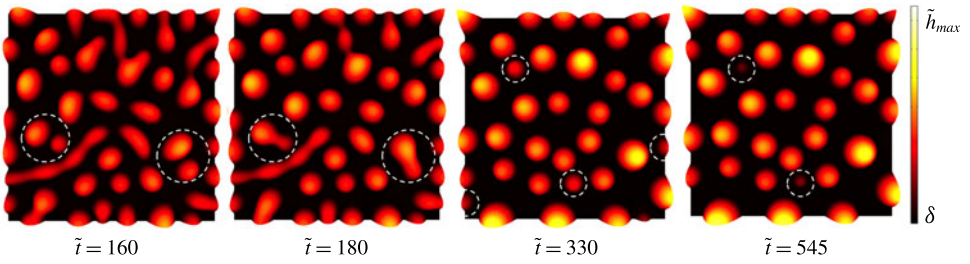


FIGURE 13. (Colour online) Two-dimensional simulations of coarsening dynamics at early and late times for the height-dependent surface tension model with $\tilde{h}_0 = 2\delta$ ($\tilde{h}_{max} = 8.5\delta$ in the colourbar). At early times, coalescence events, as highlighted by the dashed white circles, are dominant. At late times (once the metastable drops have formed), however, Ostwald ripening, i.e. capillary drainage and collapse of drops, becomes the key coarsening mechanism; note that this latter process is diffusion-dominated and therefore much slower than coarsening through coalescence events.

the classical and stochastic models. Our observations are in agreement with the 2D simulations of Glasner (2008) using a reduced-order model that suggest the dominance of the coalescence mechanism.

5.3. *Coarsening statistics*

The statistics of the coarsening process for (i) the spinodal regime, $\tilde{h}_0 = 4\delta$ (for both constant and height-dependent surface tension models as well as the classical stochastic thin-film equation with thermal noise) and (ii) for the mixed-mode instability regime $\tilde{h}_0 = 10\delta$ (for the constant surface tension model) are shown in figure 14. In the spinodal regime, the number of drops follows the scaling $N \sim \tilde{t}^{-2/5}$ in time (figure 14*a*) as computed by Glasner & Witelski (2003); incorporating the height dependence of surface tension does not alter this scaling. Introducing thermal noise does not affect the scaling either – an observation that is consistent with recent studies (Nesic *et al.* 2015). In the mixed-mode instability regime ($\tilde{h}_0 = 10\delta$), fewer drops form, so our simulations have limited statistics and do not clearly reach the self-similar intermediate regime (Gratton & Witelski 2009), but it seems that the results for this case are also in general agreement with the $\tilde{t}^{-2/5}$ scaling (figure 14*a*). Due to mass conservation, it is easy to show that the mean width of drops should then follow the scaling $\tilde{t}^{1/5}$, as shown in figure 14(*b*). An interesting feature of the variation of the mean width in time, particularly at late times, is the jumps observed as smaller drops shrink and feed into the larger drops.

As argued above, the thin-film evolution equation predicts a monotonically decreasing free energy for the system (equation (5.1)). We can further check this by looking at the variation of the numerically calculated total energy of the system $E_t \equiv \Gamma = \int \tilde{f}(\tilde{h}) + (\tilde{\kappa}/2)(\tilde{h}_{\tilde{x}})^2 \, \mathrm{d}\tilde{x}$. In agreement with the predictions of Otto *et al.* (2006), we find a $\tilde{t}^{-1/5}$ scaling for the decrease of the free energy (figure 14*c*). An interesting observation here is that for the thicker film of $\tilde{h}_0 = 10\delta$, we observe a lower total free energy at early times that later converges to the $\tilde{t}^{-1/5}$ scaling. To understand the reason behind the difference at early times, it is instructive to look at the typical variation of the different components of the free energy during the entire dewetting process, as shown in figure 14(*d*). Here, $E_b = \int \tilde{f}(\tilde{h}) \, \mathrm{d}\tilde{x}$ is the bulk free

https://doi.org/10.1017/jfm.2018.255 Published online by Cambridge University Press

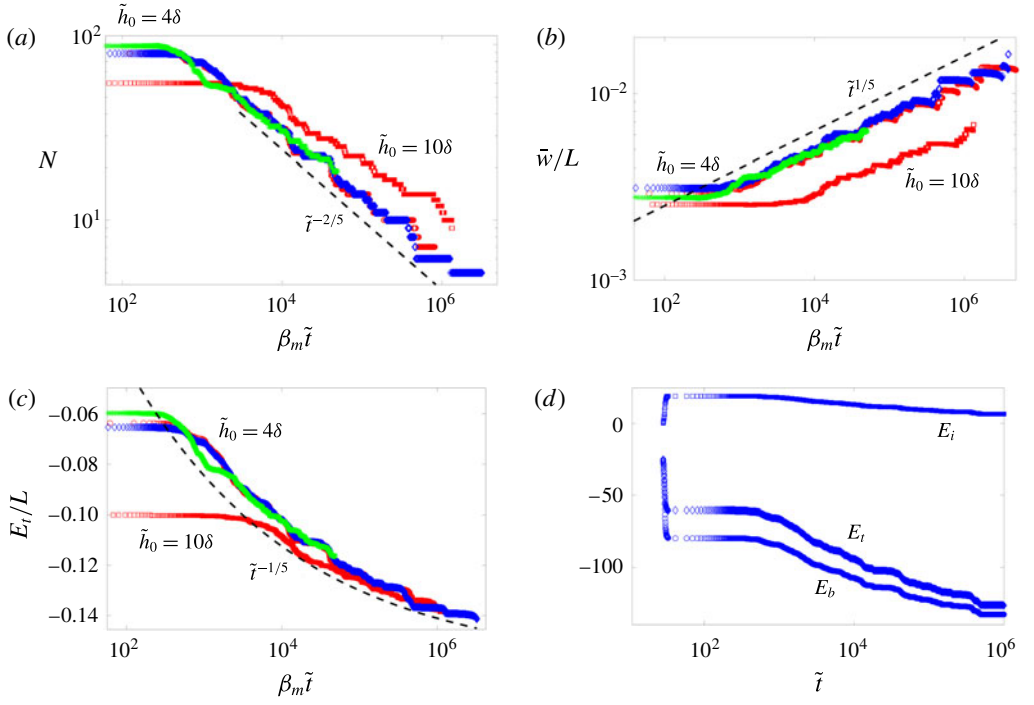


FIGURE 14. (Colour online) Coarsening statistics; red circles and squares correspond to the classical model with $\tilde{h}_0 = 4\delta$ and $\tilde{h}_0 = 10\delta$, respectively; blue diamonds show the results of the new model with $\tilde{h}_0 = 4\delta$; green stars correspond to the stochastic thin-film model with $\tilde{h}_0 = 4\delta$. (*a*) Evolution of the number of drops in time shows the scaling $\tilde{t}^{-2/5}$ as suggested by Glasner & Witelski (2003). (*b*) Evolution of mean width of drops in time; as expected from conservation of mass and the scaling of the number of drops in time, the mean width scales as $\tilde{t}^{1/5}$ in time. (*c*) Evolution of the total energy in time shows a decrease in the energy with coarsening with a scaling of $\tilde{t}^{-1/5}$, which is expected for the 1D case (Otto, Rump & Slepcev 2006); the $\tilde{h}_0 = 10\delta$ case results in fewer drops upon dewetting, therefore the majority of the domain is covered by the equilibrium film, which means the initial energy is lower than the $\tilde{h}_0 = 4\delta$ case; at long times the dynamics becomes self-similar and both follow the same scaling. (*d*) Evolution of the bulk E_b, interfacial E_i and total $E_t = E_b + E_i$ energies for a typical simulation (here $\tilde{h}_0 = 4\delta$ and height-dependent surface tension model); at short times, creation of drops increases the interfacial energy, but the total energy is still lowered due to the reduction in the bulk energy; at long times, as drops coarsen, both the bulk and interfacial energy contribution decrease.

energy and $E_i = \int(\tilde{\kappa}(\tilde{h})/2)(\tilde{h}_x)^2\,\mathrm{d}\tilde{x}$ is the interfacial energy. As an initially uniform film becomes unstable, it must increase the interfacial energy to dewet and create droplets. This increase in the interfacial energy, however, is compensated by the reduction in the bulk free energy as the ultrathin films connecting the drops are in their near-equilibrium states. The drops connected by these ultrathin films, however, are only metastable and, after a long intermediate plateau state, the system starts lowering its total energy through coarsening, which lowers both the interfacial energy as well as the bulk free energy due to the creation of new ultrathin films. With this

https://doi.org/10.1017/jfm.2018.255 Published online by Cambridge University Press

observation in mind, we can now go back to figure 14(*c*); here, the thicker film ($\tilde{h}_0 = 10\delta$) leads to the formation of fewer drops upon dewetting, meaning lower interfacial and bulk free energies in the mixed-mode instability regime compared to the spinodal regime (formation of fewer drops means a higher fraction of the total surface is covered by the ultrathin films that have a lower bulk free energy). This is why, right after dewetting, the thicker film case $\tilde{h}_0 = 10\delta$ leads to a lower total free energy compared to the $\tilde{h}_0 = 4\delta$ case in the spinodal regime. At long times, however, as the coarsening sets in, the dynamics become self-similar and the total system energies per unit length of the substrate corresponding to the different regimes all collapse on top of each other.

5.4. *LSW mean-field description of coarsening: self-similar drop-size distribution*

In the late stages of a first-order phase transition of a binary alloy mixture, Ostwald ripening is quite common (Ostwald 1897; Siggia 1979; Voorhees 1985). The curvature dependence of the chemical potential leads to a flow from higher-curvature regions (smaller clusters) to lower-curvature regions (larger clusters). The result of this coarsening is a decrease in the total interfacial energy of the system. Lifshitz & Slyozov (1961) were the first to place experimental measurements of Ostwald ripening within a consistent theoretical framework: they considered a spherical cluster in a supersaturated solution and developed a mean-field description for the evolution of the size of the cluster at long times, $\langle r(t)\rangle \sim t^{1/3}$. This scaling is an intermediate-asymptotic behaviour (Barenblatt 1996) for a quasi-steady system in isolation, i.e. the interactions with other clusters are neglected, so it is expected to hold in the limit of dilute solutions. Lifshitz & Slyozov (1961) originally assumed the transport in the medium to be diffusion-dominated; later, Wagner (1961) independently studied the Ostwald-ripening process and considered the case where the attachment/detachment of particles from the clusters is the rate-limiting factor and derived a scaling $\langle r(t)\rangle \sim t^{1/2}$. Apart from the mode of mass transport considered, the two theories are essentially the same and are known as the LSW model for coarsening (Kahlweit 1975). An alternative generalized view of the same problem is to consider all the clusters of size greater than $r_c \sim t^{\beta}$ to grow and all with a smaller size to shrink, where $\beta = 1/3$ in the diffusion-dominated case and $\beta = 1/2$ in the attachment/detachment-dominated case.

Theories of LSW type appear in many diverse phenomena, such as stability of emulsions (Imhof & Pine 1997; Taylor 1998; Bibette, Calderon & Poulin 1999; Solans *et al.* 2005; Gupta *et al.* 2016), droplet-size distribution in liquid jet fragmentation (Eggers & Villermaux 2008), coarsening of granular clusters (Aranson & Tsimring 2006), phase separation in polymer blends (Geoghegan & Krausch 2003), growth of silicone nanowires (Schmidt, Wittemann & Gösele 2010), quantum dots (Liu & Risbud 1990), growth of nanoparticles in colloidal solutions (Talapin *et al.* 2001), and grain growth in thin films (Thompson 1990), or even loss of electrocatalyst coating in low-temperature fuel cells (Shao-Horn *et al.* 2007). There is a close connection between the LSW theory and coarsening of drops connected by thin films. The drops formed upon dewetting are in a metastable quasi-equilibrium configuration, so one can treat a droplet connected to a near-equilibrium film in isolation from the other drops. The transport through the surrounding thin film is diffusion-dominated, since curvature becomes negligible in the film. Diffusion here is set by the interface potential and mobility reaches a constant value set by the film thickness, so the transport between droplets can formally be written as a diffusion equation similar to the LSW theory.

https://doi.org/10.1017/jfm.2018.255 Published online by Cambridge University Press

At long times, the clusters or drops follow a size distribution function $F(r, \tilde{t})$, or equivalently $F(m, \tilde{t})$, where $m = \int_{-\tilde{w}}^{\tilde{w}} \tilde{h}\, \mathrm{d}\tilde{x}$ is the mass of a 1D drop, which satisfies the following continuity equation (Voorhees 1985; Gratton & Witelski 2009):

$$\frac{\partial F(m, \tilde{t})}{\partial \tilde{t}} + \frac{\partial}{\partial m}(F(m, \tilde{t})v(m)) = 0, \tag{5.3}$$

where $v(m) = \mathrm{d}m/\mathrm{d}\tilde{t}$ determines the flux of particles. The number of drops can then be related to the distribution function as $N = \int_0^\infty F(m, \tilde{t})\, \mathrm{d}m$. The problem then reduces to defining the flux $v(m)$. Gratton & Witelski (2009) showed that an equivalent LSW mean-field model can be defined for a system of drops, where a drop is considered to be at a mean distance $\bar{L}(\tilde{t}) = L/N(\tilde{t})$ from two neighbouring drops of mass m_*; since the mass transport between the drops takes place through the ultrathin films with nearly zero curvature connecting them, the transport through the films becomes purely diffusive and its dynamics can be approximated as $\partial\tilde{h}/\partial\tilde{t} \sim \partial^2/\partial\tilde{x}^2(\mathcal{V}(\tilde{h}))$, where $d\mathcal{V}/\mathrm{d}\tilde{h} = \tilde{h}^3\, \mathrm{d}^2\tilde{f}/\mathrm{d}\tilde{h}^2$ (Glasner & Witelski 2003). The mean flux between the drops can then be approximated as $v(m) = 2(\mathcal{V}(m_*) - \mathcal{V}(m))/\bar{L}$, where the mean-field potential is defined as $\mathcal{V}(m_*(\tilde{t})) = (1/N)\int_0^\infty \mathcal{V}(m)F(m, \tilde{t})\, \mathrm{d}m$. The non-locality in this mean-field description comes from the mean quantities $\bar{L}$ and m_*, both of which evolve in time. At long times, we expect the distribution of the drop sizes to become self-similar, for which we can postulate $F(m, \tilde{t}) = g(m/m_*)/\tilde{t}^\alpha$ and $m_* = c\tilde{t}^\beta$. Using conservation of mass, one then arrives at the following ODE for the self-similar distribution function $g(z)$ (Gratton & Witelski 2009):

$$\frac{\mathrm{d}g}{\mathrm{d}z} = \left(\frac{27/2 - 8z^{3/2}}{4z^{5/2} + 27z(1 - \sqrt{z})}\right) g, \tag{5.4}$$

where $0 \leqslant z \equiv (m/m_*) \leqslant 9/4$, and the solution of the above equation can be obtained in the analytical form to be $g(z) = C(\sqrt{z}\mathrm{e}^{2/(-3+2\sqrt{z})})/((3 - 2\sqrt{z})^{28/9}(3 + \sqrt{z})^{17/9})$ with $C \approx 70$ as a normalization constant. From the conservation of mass, one can further find $m_* \approx 0.846\bar{m}$ (with $\bar{m} = M_{tot}/N(\tilde{t})$ being the total liquid mass divided by the instantaneous number of drops), which separates growing and shrinking drops, i.e. $v(m_*) = 0$. This mean-field treatment is expected to hold in the dilute limit, where local interactions between drops can be neglected and each drop only interacts with a background field.

The normalized distribution of the droplet mass ($\langle F(z, \tilde{t})/N(\tilde{t})\rangle >$ with $z = m/m_*$) in the self-similar intermediate regime, where the LSW model is applicable is shown in figure 15. The results of the simulations closely follow (5.4) (solid line) for small droplets. The close agreement we observe between the classical and new models, as well as in the presence of thermal fluctuations, indicates that in the self-similar coarsening regime the details of the thin-film interfacial dynamics are not critical. For larger-size droplets, i.e. $z > 1$ ($m > m_*$), however, we do observe deviations from the LSW model. While some deviations have also been observed by Gratton & Witelski (2009) in their dynamical system treatment of coarsening, and it is a known issue in the LSW model, there is a distinct skewness in the distribution of the droplets in the new model. The long tail observed in the distribution of droplet sizes in our model has also been reported in some experiments and Monte Carlo models of thin-film coarsening (Lo & Skodje 2000; Limary & Green 2002, 2003; Green 2003; Meli & Green 2008; Woehl *et al.* 2014) and is typically associated with coarsening through coalescence. This type of drop-size distribution is modelled with the Smoluchowski

https://doi.org/10.1017/jfm.2018.255 Published online by Cambridge University Press

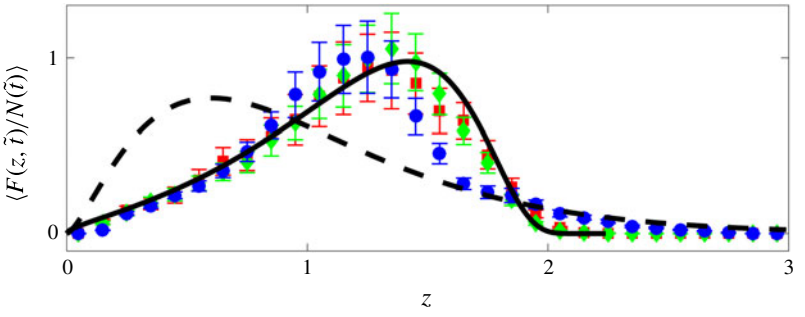


FIGURE 15. (Colour online) Droplet mass distribution for the spinodal regime with $\tilde{h}_0 = 4\delta$ obtained from ensemble averaging of 10 realizations in domains of size $250\lambda_m$ with $z = m/m_*$; vertical lines show the error bars computed from the standard deviation of the 10 realizations; red squares represent classical model with a constant surface tension; green diamonds represent the stochastic thin-film model; blue circles represent the new model wth height-dependent surface tension; the solid line represents the mean-field LSW theory (5.4); the dashed line represents the Smoluchowski distribution (5.5).

equation (Smoluchowski 1917; Sholl & Skodje 1996; Lo & Skodje 2000; Eggers & Villermaux 2008):

$$g(z) = \left(\frac{\mathrm{d}W(Wz)^{d(\alpha+1-1/d)}}{\Gamma(\alpha+1)}\right)\mathrm{e}^{-(Wz)^d}, \tag{5.5}$$

where $W = \Gamma(\alpha+1+1/d)/\Gamma(\alpha+1)$ with Γ the gamma function, and d represents the dimension of the system. When mass transport is dominated by diffusion around the periphery of the droplet, $\alpha = 3/2$; when diffusion away from the boundaries is the dominant transport mechanism, $\alpha = 1$; and when evaporation–condensation in the periphery of the drops is the main transport avenue, $\alpha = 1/2$ (Lo & Skodje 2000). Here, we find the best fit for the tail of the distribution in a 1D system of droplets is obtained for the periphery-diffusion-dominated case with $\alpha = 3/2$. It is interesting, however, that the change in the tail of the drop-size distribution in our model is not associated with a change in the coarsening mechanism, i.e. Ostwald ripening remains the dominant coarsening mechanism (figure 10); perhaps, it is the lower lateral motion of the larger-size droplets that leads to the asymmetry in the distribution. While our 1D simulation results cannot be directly compared with the experiments, the long-tailed distribution in our model calls into question whether the reported distributions in the experiments are uniquely a signature of the coalescence-dominated coarsening, and this motivates further detailed experimental observations.

6. Conclusions

We have shown, using a consistent thermodynamic framework, that the intermolecular forces between liquid–gas and liquid–solid interfaces of a thin film in the partial-wetting regime lead to an expression for the system free energy with a height-dependent surface tension. In the long-wave approximation, this free energy resembles the Cahn–Hilliard formulation for the free energy of binary alloys (Cahn & Hilliard 1958). We have shown that this new form of free energy leads to a generalized disjoining pressure that is consistent with recent calculations (Dai *et al.* 2008).

https://doi.org/10.1017/jfm.2018.255 Published online by Cambridge University Press

Using our model, we have revisited the dewetting and coarsening of thin liquid films on solid substrates in the partial-wetting regime. We have first shown that the equilibrium droplet solutions obtained in the new model have compact support and meet the contact line with a non-zero equilibrium angle, whereas equilibrium droplets in the classical model only asymptotically meet the surrounding precursor film with a zero angle. While the classical model cannot admit solutions without a precursor film (Brenner & Bertozzi 1993), our model does not require the precursor film, allowing us to recover the true partial-wetting regime (Brochard-Wyart *et al.* 1991).

Analysing the stability of uniform liquid films, we have shown that in the spinodal dewetting regime, our model predicts a faster growth rate β_m for the most unstable mode, and a smaller corresponding instability wavelength λ_m than those predicted by the classical model with a constant surface tension. While the instability wavelength is only weakly dependent on the height dependence of the surface tension, we have shown that the instability growth rate can be up to six times faster than the predictions of the classical model. This faster growth rate brings the theoretical predictions closer to the experimental observations (Becker *et al.* 2003).

Experimental observations by Limary & Green (2003) indicate a crossover in the coarsening from Ostwald-ripening-dominated to coalescence-dominated as the film thickness increases. They infer the coarsening mechanism from the droplet-size distribution, i.e. they associate the Ostwald ripening and coalescence processes with LSW-type and Smoluchowski-type distributions, respectively (Limary & Green 2002, 2003; Green 2003). Our nonlinear simulations of the dewetting and subsequent coarsening on large domains $L \sim 100\lambda_m$ have shown that the coarsening process at intermediate times becomes self-similar (Glasner & Witelski 2003) and independent of the details of the models used, i.e. we observe the same scalings for the classical model (with and without thermal noise) and in our new model with height-dependent surface tension. We have shown that the crossover reported in the experiments cannot be observed in 1D simulations of the thin-film equation. This is in contrast to the predictions of Glasner & Witelski (2005), who used a reduced-order model of thin-film equation and predicted a crossover. As the thickness of the initial uniform film increases, the instability mechanism changes from spinodal (i.e. equally distanced droplets after dewetting) to nucleation (i.e. randomly spaced droplets). This change in the instability mechanism is a result of the competition of two time scales: the growth rate of the instability, which scales as $\beta_m \sim \tilde{h}_0^{-5}$, versus the rate of lateral expansion of dewetted holes (Thiele *et al.* 2001*a*; Diez & Kondic 2007). This change of instability mechanism from spinodal to nucleation prevents the crossover from Ostwald-ripening-dominated to coalescence-dominated coarsening. We have also shown that while thermal noise enhances lateral motion of droplets, it does not lead to a crossover in the coarsening mechanism. We therefore conclude that the crossover observed in the experiments is a result of the 2D nature of the experiments versus the initial 1D simulations presented here and in earlier studies. To investigate this hypothesis, we have conducted 2D nonlinear simulations, which indeed indicate the dominance of coalescence events at early times following the dewetting, and a crossover to Ostwald ripening at late times in the coarsening process.

We also have shown that the droplet-size distribution in the self-similar coarsening regime follows a LSW-type distribution (Lifshitz & Slyozov 1961; Wagner 1961; Voorhees 1985; Gratton & Witelski 2009) and becomes model-independent, at least for small droplets. For larger drops, we have found that the new model leads to a long-tailed drop-size distribution, which follows the Smoluchowski equation (5.5) in 1D for peripheral-diffusion-dominated transport. Our observation of a skewed

https://doi.org/10.1017/jfm.2018.255 Published online by Cambridge University Press

distribution associated with an Ostwald-ripening-dominated coarsening calls into question the associations made before between the long-tailed distribution and coalescence-dominated coarsening in the earlier experiments (Limary & Green 2002, 2003; Green 2003), and motivates further detailed experimental observations.

An important open question is how to characterize the predicted height dependence of surface tension in typical dewetting experiments. As we have shown, the characteristic instability wavelength, which is most readily observed in the experiments, is only weakly dependent on the height dependence of surface tension, and perhaps not a reliable indicator. The instability growth rate, however, varies more significantly due to the height dependence of surface tension, and could serve as a distinguishing factor. Experimental measurements of growth rate are exceptionally challenging, particularly in the spinodal regime and for very thin liquid films for which the height dependence of surface tension becomes relevant. Further, the viscosity of thin polymer films changes drastically from its bulk values due to a shift in the glass transition temperature (Herminghaus, Jacobs & Seemann 2001), making it potentially difficult to distinguish the consequences of the changes in surface tension from those of the changes in viscosity. Spreading of droplets in the partial-wetting regime can therefore serve as an alternative test for the height dependence of surface tension; we have shown that our new model allows investigations of the spreading process without the need for precursor films (Pahlavan *et al.* 2015). Visualization of the contact-line motion at micro/nanoscales (Chen, Yu & Wang 2014; Qian, Park & Breuer 2015; Deng *et al.* 2016; McGraw *et al.* 2016) could therefore lead the way in refining and validating models for interfacial flows.

REFERENCES

AMIRFAZLI, A. & NEUMANN, A. W. 2004 Status of the three-phase line tension: a review. *Adv. Colloid Interface Sci.* **110** (3), 121–141.

ANDERSON, D. M., MCFADDEN, G. B. & WHEELER, A. A. 1998 Diffuse-interface methods in fluid mechanics. *Annu. Rev. Fluid Mech.* **30** (1), 139–165.

ARANSON, I. S. & TSIMRING, L. S. 2006 Patterns and collective behavior in granular media: theoretical concepts. *Rev. Mod. Phys.* **78**, 641–692.

ARFKEN, G. B., WEBER, H. J. & HARRIS, F. E. (Eds) 2013 *Mathematical Methods for Physicists*, 7th edn. Academic Press.

BARENBLATT, G. I. 1996 *Scaling, Self-similarity, and Intermediate Asymptotics: Dimensional Analysis and Intermediate Asymptotics*. Cambridge University Press.

BAUER, C. & DIETRICH, S. 1999 Quantitative study of laterally inhomogeneous wetting films. *Eur. Phys. J.* B **10** (4), 767–779.

BÄUMCHEN, O., FETZER, R., KLOS, M., LESSEL, M., MARQUANT, L., HÄHL, H. & JACOBS, K. 2012 Slippage and nanorheology of thin liquid polymer films. *J. Phys.: Condens. Matter* **24** (32), 325102.

BÄUMCHEN, O. & JACOBS, K. 2010 Slip effects in polymer thin films. *J. Phys.: Condens. Matter* **22** (3), 033102.

BÄUMCHEN, O., MARQUANT, L., BLOSSEY, R., MÜNCH, A., WAGNER, B. & JACOBS, K. 2014 Influence of slip on the Rayleigh–Plateau rim instability in dewetting viscous films. *Phys. Rev. Lett.* **113**, 014501.

BECKER, J., GRUN, G., SEEMANN, R., MANTZ, H., JACOBS, K., MECKE, K. R. & BLOSSEY, R. 2003 Complex dewetting scenarios captured by thin-film models. *Nat. Mater.* **2** (1), 59–63.

BELARDINELLI, D., SBRAGAGLIA, M., GROSS, M. & ANDREOTTI, B. 2016 Thermal fluctuations of an interface near a contact line. *Phys. Rev.* E **94**, 052803.

BENZI, R., SBRAGAGLIA, M., BERNASCHI, M. & SUCCI, S. 2011 Phase-field model of long-time glasslike relaxation in binary fluid mixtures. *Phys. Rev. Lett.* **106**, 164501.

https://doi.org/10.1017/jfm.2018.255 Published online by Cambridge University Press

BERTOZZI, A. L., GRÜN, G. & WITELSKI, T. P. 2001 Dewetting films: bifurcations and concentrations. *Nonlinearity* **14** (6), 1569–1592.

BIBETTE, J., CALDERON, F. L. & POULIN, P. 1999 Emulsions: basic principles. *Rep. Prog. Phys.* **62** (6), 969–1033.

BISCHOF, J., SCHERER, D., HERMINGHAUS, S. & LEIDERER, P. 1996 Dewetting modes of thin metallic films: nucleation of holes and spinodal dewetting. *Phys. Rev. Lett.* **77**, 1536–1539.

BLAKE, T. D. & RUSCHAK, K. J. 1979 A maximum speed of wetting. *Nature* **282** (5738), 489–491.

BLOSSEY, R. 2012 *Thin Liquid Films: Dewetting and Polymer Flow*. Springer.

BOCQUET, L. & CHARLAIX, E. 2010 Nanofluidics, from bulk to interfaces. *Chem. Soc. Rev.* **39**, 1073–1095.

BOCQUET, L. & TABELING, P. 2014 Physics and technological aspects of nanofluidics. *Lab on a Chip* **14**, 3143–3158.

BOLLINNE, C., CUENOT, S., NYSTEN, B. & JONAS, A. M. 2003 Spinodal-like dewetting of thermodynamically-stable thin polymer films. *Eur. Phys. J.* E **12** (3), 389–396.

BONN, D., EGGERS, J., INDEKEU, J., MEUNIER, J. & ROLLEY, E. 2009 Wetting and spreading. *Rev. Mod. Phys.* **81**, 739–805.

BRAUN, R. J. 2012 Dynamics of the tear film. *Annu. Rev. Fluid Mech.* **44** (1), 267–297.

BRAY, A. J. 2002 Theory of phase-ordering kinetics. *Adv. Phys.* **51** (2), 481–587.

BRENNER, M. & BERTOZZI, A. 1993 Spreading of droplets on a solid surface. *Phys. Rev. Lett.* **71**, 593–596.

BROCHARD-WYART, F., DI MEGLIO, J. M., QUERE, D. & DE GENNES, P.-G. 1991 Spreading of nonvolatile liquids in a continuum picture. *Langmuir* **7** (2), 335–338.

BROCHARD-WYART, F., MARTIN, P. & REDON, C. 1993 Liquid/liquid dewetting. *Langmuir* **9** (12), 3682–3690.

CAHN, J. W. 1961 On spinodal decomposition. *Acta Metall.* **9** (9), 795–801.

CAHN, J. W. & HILLIARD, J. E. 1958 Free energy of a nonuniform system. i. Interfacial free energy. *J. Chem. Phys.* **28** (2), 258–267.

CHEN, J.-T., ZHANG, M. & RUSSELL, T. P. 2007 Instabilities in nanoporous media. *Nano Lett.* **7** (1), 183–187.

CHEN, L., YU, J. & WANG, H. 2014 Convex nanobending at a moving contact line: the missing mesoscopic link in dynamic wetting. *ACS Nano* **8** (11), 11493–11498.

COLIN, A., SQUIRES, T. M. & BOCQUET, L. 2012 Soft matter principles of microfluidics. *Soft Matt.* **8**, 10527–10529.

CRASTER, R. V. & MATAR, O. K. 2009 Dynamics and stability of thin liquid films. *Rev. Mod. Phys.* **81**, 1131–1198.

CROSS, M. C. & HOHENBERG, P. C. 1993 Pattern formation outside of equilibrium. *Rev. Mod. Phys.* **65**, 851–1112.

CUETO-FELGUEROSO, L. & JUANES, R. 2012 Macroscopic phase-field model of partial wetting: bubbles in a capillary tube. *Phys. Rev. Lett.* **108**, 144502.

DAI, B., LEAL, L. G. & REDONDO, A. 2008 Disjoining pressure for nonuniform thin films. *Phys. Rev.* E **78**, 061602.

DAVIDOVITCH, B., MORO, E. & STONE, H. A. 2005 Spreading of viscous fluid drops on a solid substrate assisted by thermal fluctuations. *Phys. Rev. Lett.* **95**, 244505.

DENG, Y., CHEN, L., LIU, Q., YU, J. & WANG, H. 2016 Nanoscale view of dewetting and coating on partially wetted solids. *J. Phys. Chem. Lett.* **7** (10), 1763–1768.

DIEZ, J. A., GONZÁLEZ, A. G. & FERNÁNDEZ, R. 2016 Metallic-thin-film instability with spatially correlated thermal noise. *Phys. Rev.* E **93**, 013120.

DIEZ, J. A. & KONDIC, L. 2007 On the breakup of fluid films of finite and infinite extent. *Phys. Fluids* **19** (7), 072107.

DZYALOSHINSKII, I. E., LIFSHITZ, E. M. & PITAEVSKII, L. P. 1961 The general theory of van der Waals forces. *Adv. Phys.* **10** (38), 165–209.

EGGERS, J. & VILLERMAUX, E. 2008 Physics of liquid jets. *Rep. Prog. Phys.* **71** (3), 036601.

FETZER, R., JACOBS, K., MÜNCH, A., WAGNER, B. & WITELSKI, T. P. 2005 New slip regimes and the shape of dewetting thin liquid films. *Phys. Rev. Lett.* **95**, 127801.

https://doi.org/10.1017/jfm.2018.255 Published online by Cambridge University Press

FETZER, R., MÜNCH, A., WAGNER, B., RAUSCHER, M. & JACOBS, K. 2007*a* Quantifying hydrodynamic slip: a comprehensive analysis of dewetting profiles. *Langmuir* **23** (21), 10559–10566.

FETZER, R., RAUSCHER, M., SEEMANN, R., JACOBS, K. & MECKE, K. 2007*b* Thermal noise influences fluid flow in thin films during spinodal dewetting. *Phys. Rev. Lett.* **99**, 114503.

FOWLKES, J. D., KONDIC, L., DIEZ, J., WU, Y. & RACK, P. D. 2011 Self-assembly versus directed assembly of nanoparticles via pulsed laser induced dewetting of patterned metal films. *Nano Lett.* **11** (6), 2478–2485.

GATES, B. D., XU, Q., STEWART, M., RYAN, D., WILLSON, C. G. & WHITESIDES, G. M. 2005 New approaches to nanofabrication: molding, printing, and other techniques. *Chem. Rev.* **105** (4), 1171–1196.

GAU, H., HERMINGHAUS, S., LENZ, P. & LIPOWSKY, R. 1999 Liquid morphologies on structured surfaces: from microchannels to microchips. *Science* **283** (5398), 46–49.

DE GENNES, P.-G. 1980 Dynamics of fluctuations and spinodal decomposition in polymer blends. *J. Chem. Phys.* **72** (9), 4756–4763.

DE GENNES, P.-G. 1985 Wetting: statics and dynamics. *Rev. Mod. Phys.* **57**, 827–863.

DE GENNES, P.-G., BROCHARD-WYART, F. & QUÉRÉ, D. 2004 *Capillarity and Wetting Phenomena: Drops, Bubbles, Pearls, Waves*. Springer.

GENTILI, D., FOSCHI, G., VALLE, F., CAVALLINI, M. & BISCARINI, F. 2012 Applications of dewetting in micro and nanotechnology. *Chem. Soc. Rev.* **41**, 4430–4443.

GEOGHEGAN, M. & KRAUSCH, G. 2003 Wetting at polymer surfaces and interfaces. *Prog. Polym. Sci.* **28** (2), 261–302.

GETTA, T. & DIETRICH, S. 1998 Line tension between fluid phases and a substrate. *Phys. Rev.* E **57**, 655–671.

GIRO, R., BRYANT, P. W., ENGEL, M., NEUMANN, R. F. & STEINER, M. B. 2017 Adsorption energy as a metric for wettability at the nanoscale. *Sci. Rep.* **7** (46317).

GLASNER, K. 2008 Ostwald ripening in thin film equations. *SIAM J. Appl. Maths* **69** (2), 473–493.

GLASNER, K. B. & WITELSKI, T. P. 2005 Collision versus collapse of droplets in coarsening of dewetting thin films. *Physica* D **209** (1–4), 80–104.

GLASNER, K. B. & WITELSKI, T. P. 2003 Coarsening dynamics of dewetting films. *Phys. Rev.* E **67**, 016302.

GOGOTSI, Y., LIBERA, J. A., GÜVENÇ-YAZICIOGLU, A. & MEGARIDIS, C. M. 2001 *In situ* multiphase fluid experiments in hydrothermal carbon nanotubes. *Appl. Phys. Lett.* **79** (7), 1021–1023.

GRANICK, S., ZHU, Y. & LEE, H. 2003 Slippery questions about complex fluids flowing past solids. *Nat. Mater.* **2** (4), 221–227.

GRATTON, M. B. 2008 coarsening of thin fluid films. PhD thesis, Department of Mathematics, Duke University.

GRATTON, M. B. & WITELSKI, T. P. 2008 Coarsening of unstable thin films subject to gravity. *Phys. Rev.* E **77**, 016301.

GRATTON, M. B. & WITELSKI, T. P. 2009 Transient and self-similar dynamics in thin film coarsening. *Physica* D **238** (23–24), 2380–2394.

GREEN, P. F. 2003 Wetting and dynamics of structured liquid films. *J. Polym. Sci.* B **41** (19), 2219–2235.

GRÜN, G., MECKE, K. & RAUSCHER, M. 2006 Thin-film flow influenced by thermal noise. *J. Stat. Phys.* **122** (6), 1261–1291.

GUPTA, A., ERAL, H. B., HATTON, T. A. & DOYLE, P. S. 2016 Nanoemulsions: formation, properties and applications. *Soft Matt.* **12**, 2826–2841.

VAN HAMEREN, R., SCHÖN, P., VAN BUUL, A. M., HOOGBOOM, J., LAZARENKO, S. V., GERRITSEN, J. W., ENGELKAMP, H., CHRISTIANEN, P. C. M., HEUS, H. A., MAAN, J. C., RASING, T., SPELLER, S., ROWAN, A. E., ELEMANS, J. A. A. W. & NOLTE, R. J. M. 2006 Macroscopic hierarchical surface patterning of porphyrin trimers via self-assembly and dewetting. *Science* **314** (5804), 1433.

https://doi.org/10.1017/jfm.2018.255 Published online by Cambridge University Press

HAMMOUD, N. H., TRINH, P. H., HOWELL, P. D. & STONE, H. A. 2017 Influence of van der Waals forces on a bubble moving in a tube. *Phys. Rev. Fluids* **2**, 063601.

HAN, W. & LIN, Z. 2012 Learning from 'coffee rings': ordered structures enabled by controlled evaporative self-assembly. *Angew. Chem. Intl Ed. Engl.* **51** (7), 1534–1546.

HERMINGHAUS, S., JACOBS, K., MECKE, K., BISCHOF, J., FERY, A., IBN-ELHAJ, M. & SCHLAGOWSKI, S. 1998 Spinodal dewetting in liquid crystal and liquid metal films. *Science* **282** (5390), 916–919.

HERMINGHAUS, S., JACOBS, K. & SEEMANN, R. 2001 The glass transition of thin polymer films: some questions, and a possible answer. *Eur. Phys. J.* E **5** (1), 531–538.

HERMINGHAUS, S., SEEMANN, R. & JACOBS, K. 2002 Generic morphologies of viscoelastic dewetting fronts. *Phys. Rev. Lett.* **89**, 056101.

HESLOT, F., CAZABAT, A. M., LEVINSON, P. & FRAYSSE, N. 1990 Experiments on wetting on the scale of nanometers: influence of the surface energy. *Phys. Rev. Lett.* **65**, 599–602.

HIGGINS, A. M. & JONES, R. A. L. 2000 Anisotropic spinodal dewetting as a route to self-assembly of patterned surfaces. *Nature* **404** (6777), 476–478.

HOCKING, L. M. 1993 The influence of intermolecular forces on thin fluid layers. *Phys. Fluids* A **5** (4), 793–799.

HOHENBERG, P. C. & HALPERIN, B. I. 1977 Theory of dynamic critical phenomena. *Rev. Mod. Phys.* **49**, 435–479.

HUANG, J., KIM, F., TAO, A. R., CONNOR, S. & YANG, P. 2005 Spontaneous formation of nanoparticle stripe patterns through dewetting. *Nat. Mater.* **4** (12), 896–900.

HUANG, J. Y., LO, Y.-C., NIU, J. J., KUSHIMA, A., QIAN, X., ZHONG, L., MAO, S. X. & LI, J. 2013 Nanowire liquid pumps. *Nat. Nanotechnol.* **8** (4), 277–281.

HUERRE, A., THEODOLY, O., LESHANSKY, A. M., VALIGNAT, M.-P., CANTAT, I. & JULLIEN, M.-C. 2015 Droplets in microchannels: dynamical properties of the lubrication film. *Phys. Rev. Lett.* **115**, 064501.

IMHOF, A. & PINE, D. J. 1997 Stability of nonaqueous emulsions. *J. Colloid Interface Sci.* **192** (2), 368–374.

INDEIKINA, A. & CHANG, H.-C. 1999 A molecular theory for dynamic contact angles. In *IUTAM Symposium on Non-linear Singularities in Deformation and Flow: Proceedings of the IUTAM Symposium held in Haifa, Israel 17–21 March 1997* (ed. D. Durban & J. R. A. Pearson), pp. 321–337. Springer.

ISRAELACHVILI, J. N. 2011 *Intermolecular and Surface Forces*. Academic Press.

JACOBS, K., HERMINGHAUS, S. & MECKE, K. R. 1998 Thin liquid polymer films rupture via defects. *Langmuir* **14** (4), 965–969.

KAHLWEIT, M. 1975 Ostwald ripening of precipitates. *Adv. Colloid Interface Sci.* **5** (1), 1–35.

KARDAR, M., PARISI, G. & ZHANG, Y.-C. 1986 Dynamic scaling of growing interfaces. *Phys. Rev. Lett.* **56**, 889–892.

KEISER, L., BENSE, H., COLINET, P., BICO, J. & REYSSAT, E. 2017 Marangoni bursting: evaporation-induced emulsification of binary mixtures on a liquid layer. *Phys. Rev. Lett.* **118**, 074504.

KELLER, J. B. & MERCHANT, G. J. 1991 Flexural rigidity of a liquid surface. *J. Stat. Phys.* **63** (5–6), 1039–1051.

KONG, Y. L., BOULOGNE, F., KIM, H., NUNES, J., FENG, J. & STONE, H. A. 2015 Deposition of quantum dots in a capillary tube. *Langmuir* **31** (45), 12560–12566.

KONG, Y. L., GUPTA, M. K., JOHNSON, B. N. & MCALPINE, M. C. 2016 3D printed bionic nanodevices. *Nano Today* **11** (3), 330–350.

KUMAR, S. 2015 Liquid transfer in printing processes: liquid bridges with moving contact lines. *Annu. Rev. Fluid Mech.* **47** (1), 67–94.

KUNDAN, A., NGUYEN, T. T. T., PLAWSKY, J. L., WAYNER, P. C., CHAO, D. F. & SICKER, R. J. 2017 Condensation on highly superheated surfaces: unstable thin films in a wickless heat pipe. *Phys. Rev. Lett.* **118**, 094501.

LANGER, J. S. 1971 Theory of spinodal decomposition in alloys. *Ann. Phys.* **65** (1), 53–86.

LAUGA, E., BRENNER, M. & STONE, H. 2007 *Microfluidics: The No-Slip Boundary Condition*. pp. 1219–1240. Springer.

https://doi.org/10.1017/jfm.2018.255 Published online by Cambridge University Press

LEAL, L. G. 2004 Flow induced coalescence of drops in a viscous fluid. *Phys. Fluids* **16** (6), 1833–1851.

LI, J. 2016 Macroscopic model for head-on binary droplet collisions in a gaseous medium. *Phys. Rev. Lett.* **117**, 214502.

LIFSHITZ, I. M. & SLYOZOV, V. V. 1961 The kinetics of precipitation from supersaturated solid solutions. *J. Phys. Chem. Solids* **19** (1), 35–50.

LIMARY, R. & GREEN, P. F. 2002 Late-stage coarsening of an unstable structured liquid film. *Phys. Rev.* E **66**, 021601.

LIMARY, R. & GREEN, P. F. 2003 Dynamics of droplets on the surface of a structured fluid film: late-stage coarsening. *Langmuir* **19** (6), 2419–2424.

LIU, L. & RISBUD, S. H. 1990 Quantum-dot size-distribution analysis and precipitation stages in semiconductor doped glasses. *J. Appl. Phys.* **68** (1), 28–32.

LO, A. & SKODJE, R. T. 2000 Kinetic and Monte Carlo models of thin film coarsening: cross over from diffusion-coalescence to Ostwald growth modes. *J. Chem. Phys.* **112** (4), 1966–1974.

LOHSE, D. & ZHANG, X. 2015 Surface nanobubbles and nanodroplets. *Rev. Mod. Phys.* **87**, 981–1035.

LOPES, W. A. & JAEGER, H. M. 2001 Hierarchical self-assembly of metal nanostructures on diblock copolymer scaffolds. *Nature* **414** (6865), 735–738.

MACDOWELL, L. G., BENET, J. & KATCHO, N. A. 2013 Capillary fluctuations and film-height-dependent surface tension of an adsorbed liquid film. *Phys. Rev. Lett.* **111**, 047802.

MACDOWELL, L. G., BENET, J., KATCHO, N. A. & PALANCO, J. M. G. 2014 Disjoining pressure and the film-height-dependent surface tension of thin liquid films: new insight from capillary wave fluctuations. *Adv. Colloid Interface Sci.* **206**, 150–171.

MANTZ, H., JACOBS, K. & MECKE, K. 2008 Utilizing Minkowski functionals for image analysis: a marching square algorithm. *J. Stat. Mech.: Theory Exp.* **2008** (12), P12015.

MARCHAND, A., WEIJS, J. H., SNOEIJER, J. H. & ANDREOTTI, B. 2011 Why is surface tension a force parallel to the interface? *Am. J. Phys.* **79** (10), 999–1008.

MCGRAW, J. D., BÄUMCHEN, O., KLOS, M., HAEFNER, S., LESSEL, M., BACKES, S. & JACOBS, K. 2014 Nanofluidics of thin polymer films: linking the slip boundary condition at solid–liquid interfaces to macroscopic pattern formation and microscopic interfacial properties. *Adv. Colloid Interface Sci.* **210**, 13–20.

MCGRAW, J. D., CHAN, T. S., MAURER, S., SALEZ, T., BENZAQUEN, M., RAPHAËL, E., BRINKMANN, M. & JACOBS, K. 2016 Slip-mediated dewetting of polymer microdroplets. *Proc. Natl Acad. Sci. USA* **113** (5), 1168–1173.

MCKEOWN, J. T., WU, Y., FOWLKES, J. D., RACK, P. D. & CAMPBELL, G. H. 2015 Simultaneous *in-situ* synthesis and characterization of co@cu core-shell nanoparticle arrays. *Adv. Mater.* **27** (6), 1060–1065.

MECKE, K. & RAUSCHER, M. 2005 On thermal fluctuations in thin film flow. *J. Phys.: Condens. Matter* **17** (45), S3515.

MECKE, K. R. 1998 Integral geometry in statistical physics. *Intl J. Mod. Phys.* B **12** (09), 861–899.

MELI, L. & GREEN, P. F. 2008 Aggregation and coarsening of ligand-stabilized gold nanoparticles in poly(methyl methacrylate) thin films. *ACS Nano* **2** (6), 1305–1312.

MERCHANT, G. J. & KELLER, J. B. 1992 Contact angles. *Phys. Fluids* A **4** (3), 477–485.

MEREDITH, J. C., SMITH, A. P., KARIM, A. & AMIS, E. J. 2000 Combinatorial materials science for polymer thin-film dewetting. *Macromolecules* **33** (26), 9747–9756.

MILLER, C. A. & RUCKENSTEIN, E. 1974 The origin of flow during wetting of solids. *J. Colloid Interface Sci.* **48** (3), 368–373.

MITLIN, V. S. 1993 Dewetting of solid surface: analogy with spinodal decomposition. *J. Colloid Interface Sci.* **156** (2), 491–497.

MOLARES, M. E. T., BALOGH, A. G., CORNELIUS, T. W., NEUMANN, R. & TRAUTMANN, C. 2004 Fragmentation of nanowires driven by Rayleigh instability. *Appl. Phys. Lett.* **85** (22), 5337–5339.

MUKHERJEE, R. & SHARMA, A. 2015 Instability, self-organization and pattern formation in thin soft films. *Soft Matt.* **11**, 8717–8740.

https://doi.org/10.1017/jfm.2018.255 Published online by Cambridge University Press

NESIC, S., CUERNO, R., MORO, E. & KONDIC, L. 2015 Fully nonlinear dynamics of stochastic thin-film dewetting. *Phys. Rev.* E **92**, 061002.

NETO, C., EVANS, D. R., BONACCURSO, E., BUTT, H.-J. & CRAIG, V. S. J. 2005 Boundary slip in Newtonian liquids: a review of experimental studies. *Rep. Prog. Phys.* **68** (12), 2859.

NETO, C., JACOBS, K., SEEMANN, R., BLOSSEY, R., BECKER, J. & GRÜN, G. 2003 Satellite hole formation during dewetting: experiment and simulation. *J. Phys.: Condens. Matter* **15** (19), 3355–3366.

NGUYEN, T. D., FUENTES-CABRERA, M., FOWLKES, J. D. & RACK, P. D. 2014 Coexistence of spinodal instability and thermal nucleation in thin-film rupture: insights from molecular levels. *Phys. Rev.* E **89**, 032403.

NOVICK-COHEN, A. 1985 The nonlinear Cahn–Hilliard equation: transition from spinodal decomposition to nucleation behavior. *J. Stat. Phys.* **38** (3), 707–723.

ORON, A. 2000 Three-dimensional nonlinear dynamics of thin liquid films. *Phys. Rev. Lett.* **85**, 2108–2111.

ORON, A., DAVIS, S. H. & BANKOFF, S. G. 1997 Long-scale evolution of thin liquid films. *Rev. Mod. Phys.* **69**, 931–980.

OSTWALD, W. 1897 Studien über die Bildung und Umwandlung fester Körper: Übersättigung und Überkaltung. *Z. Phys. Chem.* **22**, 289–330.

OTTO, F., RUMP, T. & SLEPCEV, D. 2006 Coarsening rates for a droplet model: rigorous upper bounds. *SIAM J. Math. Anal.* **38** (2), 503–529.

PAHLAVAN, A. A., CUETO-FELGUEROSO, L., MCKINLEY, G. H. & JUANES, R. 2015 Thin films in partial wetting: internal selection of contact-line dynamics. *Phys. Rev. Lett.* **115**, 034502.

PIERRE-LOUIS, O. 2016 Solid-state wetting at the nanoscale. *Prog. Cryst. Growth Charact. Mater.* **62** (2), 177–202.

POKROY, B., KANG, S. H., MAHADEVAN, L. & AIZENBERG, J. 2009 Self-organization of a mesoscale bristle into ordered, hierarchical helical assemblies. *Science* **323** (5911), 237–240.

POMPE, T. & HERMINGHAUS, S. 2000 Three-phase contact line energetics from nanoscale liquid surface topographies. *Phys. Rev. Lett.* **85**, 1930–1933.

QIAN, B., PARK, J. & BREUER, K. S. 2015 Large apparent slip at a moving contact line. *Phys. Fluids* **27** (9), 091703.

QIN, D., XIA, Y. & WHITESIDES, G. M. 2010 Soft lithography for micro- and nanoscale patterning. *Nat. Protocols* **5** (3), 491–502.

QUÉRÉ, D. 1999 Fluid coating on a fiber. *Annu. Rev. Fluid Mech.* **31** (1), 347–384.

RAUSCHER, M. & DIETRICH, S. 2008 Wetting phenomena in nanofluidics. *Annu. Rev. Mater. Res.* **38** (1), 143–172.

REITER, G. 1992 Dewetting of thin polymer films. *Phys. Rev. Lett.* **68**, 75–78.

REITER, G. 1993 Unstable thin polymer films: rupture and dewetting processes. *Langmuir* **9** (5), 1344–1351.

REITER, G., HAMIEH, M., DAMMAN, P., SCLAVONS, S., GABRIELE, S., VILMIN, T. & RAPHAEL, E. 2005 Residual stresses in thin polymer films cause rupture and dominate early stages of dewetting. *Nat. Mater.* **4** (10), 754–758.

REITER, G. & SHARMA, A. 2001 Auto-optimization of dewetting rates by rim instabilities in slipping polymer films. *Phys. Rev. Lett.* **87**, 166103.

REYNOLDS, O. 1886 On the theory of lubrication and its application to Mr. Beauchamp Tower's experiments, including an experimental determination of the viscosity of olive oil. *Phil. Trans. R. Soc. Lond.* **177**, 157–234.

ROWLINSON, J. S. 1979 Translation of J. D. van der Waals' 'The thermodynamik theory of capillarity under the hypothesis of a continuous variation of density'. *J. Stat. Phys.* **20** (2), 197–200.

ROWLINSON, J. S. & WIDOM, B. 2013 *Molecular Theory of Capillarity*. Courier Corporation.

RUCKENSTEIN, E. & JAIN, R. K. 1974 Spontaneous rupture of thin liquid films. *J. Chem. Soc. Faraday Trans. II* **70**, 132–147.

RUSCHAK, K. J. 1985 Coating flows. *Annu. Rev. Fluid Mech.* **17** (1), 65–89.

SCHIMMELE, L., NAPIORKOWSKI, M. & DIETRICH, S. 2007 Conceptual aspects of line tensions. *J. Chem. Phys.* **127** (16), 164715.

https://doi.org/10.1017/jfm.2018.255 Published online by Cambridge University Press

SCHMIDT, V., WITTEMANN, J. V. & GÖSELE, U. 2010 Growth, thermodynamics, and electrical properties of silicon nanowires. *Chem. Rev.* **110** (1), 361–388.

SCHOCH, R. B., HAN, J. & RENAUD, P. 2008 Transport phenomena in nanofluidics. *Rev. Mod. Phys.* **80**, 839–883.

SEEMANN, R., HERMINGHAUS, S. & JACOBS, K. 2001*a* Dewetting patterns and molecular forces: a reconciliation. *Phys. Rev. Lett.* **86**, 5534–5537.

SEEMANN, R., HERMINGHAUS, S. & JACOBS, K. 2001*b* Shape of a liquid front upon dewetting. *Phys. Rev. Lett.* **87**, 196101.

SEEMANN, R., HERMINGHAUS, S., NETO, C., SCHLAGOWSKI, S., PODZIMEK, D., KONRAD, R., MANTZ, H. & JACOBS, K. 2005 Dynamics and structure formation in thin polymer melt films. *J. Phys.: Condens. Matter* **17** (9), S267.

SEGALMAN, R. A. 2005 Patterning with block copolymer thin films. *Mater. Sci. Engng* **48** (6), 191–226.

SEGALMAN, R. A. & GREEN, P. F. 1999 Dynamics of rims and the onset of spinodal dewetting at liquid/liquid interfaces. *Macromolecules* **32** (3), 801–807.

SHAO-HORN, Y., SHENG, W. C., CHEN, S., FERREIRA, P. J., HOLBY, E. F. & MORGAN, D. 2007 Instability of supported platinum nanoparticles in low-temperature fuel cells. *Top. Catal.* **46** (3), 285–305.

SHARMA, A. 1993*a* Equilibrium contact angles and film thicknesses in the apolar and polar systems: role of intermolecular interactions in coexistence of drops with thin films. *Langmuir* **9** (12), 3580–3586.

SHARMA, A. 1993*b* Relationship of thin film stability and morphology to macroscopic parameters of wetting in the apolar and polar systems. *Langmuir* **9** (3), 861–869.

SHARMA, A. 2003 Many paths to dewetting of thin films: anatomy and physiology of surface instability. *Eur. Phys. J.* E **12** (3), 397–408.

SHARMA, A. & KHANNA, R. 1998 Pattern formation in unstable thin liquid films. *Phys. Rev. Lett.* **81**, 3463–3466.

SHARMA, A. & REITER, G. 1996 Instability of thin polymer films on coated substrates: rupture, dewetting, and drop formation. *J. Colloid Interface Sci.* **178** (2), 383–399.

SHELUDKO, A. 1967 Thin liquid films. *Adv. Colloid Interface Sci.* **1** (4), 391–464.

SHIKHMURZAEV, Y. D. 1997 Moving contact lines in liquid/liquid/solid systems. *J. Fluid Mech.* **334**, 211–249.

SHIKHMURZAEV, Y. D. 2007 *Capillary Flows with Forming Interfaces*. CRC Press.

SHOLL, D. S. & SKODJE, R. T. 1996 Late-stage coarsening of adlayers by dynamic cluster coalescence. *Physica* A **231** (4), 631–647.

SIBLEY, D., SAVVA, N. & KALLIADASIS, S. 2012 Slip or not slip? a methodical examination of the interface formation model using two-dimensional droplet spreading on a horizontal planar substrate as a prototype system. *Phys. Fluids* **24** (8), 082105.

SIBLEY, D. N., NOLD, A., SAVVA, N. & KALLIADASIS, S. 2015 A comparison of slip, disjoining pressure, and interface formation models for contact line motion through asymptotic analysis of thin two-dimensional droplet spreading. *J. Engng Maths* **94** (1), 19–41.

SIGGIA, E. D. 1979 Late stages of spinodal decomposition in binary mixtures. *Phys. Rev.* A **20**, 595–605.

SMOLUCHOWSKI, M. V. 1917 Grundriß der Koagulationskinetik kolloider Lösungen. *Colloid Polym. Sci.* **21** (3), 98–104.

SNOEIJER, J. H. & ANDREOTTI, B. 2008 A microscopic view on contact angle selection. *Phys. Fluids* **20** (5), 057101.

SNOEIJER, J. H. & ANDREOTTI, B. 2013 Moving contact lines: scales, regimes, and dynamical transitions. *Annu. Rev. Fluid Mech.* **45** (1), 269–292.

SNOEIJER, J. H. & EGGERS, J. 2010 Asymptotic analysis of the dewetting rim. *Phys. Rev.* E **82**, 056314.

SOLANS, C., IZQUIERDO, P., NOLLA, J., AZEMAR, N. & GARCIA-CELMA, M. J. 2005 Nano-emulsions. *Curr. Opin. Colloid Interface Sci.* **10** (3–4), 102–110.

https://doi.org/10.1017/jfm.2018.255 Published online by Cambridge University Press

SQUIRES, T. M. & QUAKE, S. R. 2005 Microfluidics: fluid physics at the nanoliter scale. *Rev. Mod. Phys.* **77**, 977–1026.

STANGE, T. G., EVANS, D. F. & HENDRICKSON, W. A. 1997 Nucleation and growth of defects leading to dewetting of thin polymer films. *Langmuir* **13** (16), 4459–4465.

STAROV, V. M. 2010 Surface forces action in a vicinity of three phase contact line and other current problems in kinetics of wetting and spreading. *Adv. Colloid Interface Sci.* **161** (1–2), 139–152.

STAROV, V. M., VELARDE, M. G. & RADKE, C. J. 2007 *Wetting and Spreading Dynamics*. CRC Press.

STENHAMMAR, J., TIRIBOCCHI, A., ALLEN, R. J., MARENDUZZO, D. & CATES, M. E. 2013 Continuum theory of phase separation kinetics for active Brownian particles. *Phys. Rev. Lett.* **111**, 145702.

STONE, H. A., STROOCK, A. D. & AJDARI, A. 2004 Engineering flows in small devices. *Annu. Rev. Fluid Mech.* **36** (1), 381–411.

TALAPIN, D. V., ROGACH, A. L., HAASE, M. & WELLER, H. 2001 Evolution of an ensemble of nanoparticles in a colloidal solution: theoretical study. *J. Phys. Chem.* B **105** (49), 12278–12285.

TAO, Y., YECKEL, A. & DERBY, J. J. 2016 Steady-state and dynamic models for particle engulfment during solidification. *J. Comput. Phys.* **315**, 238–263.

TAYLOR, P. 1998 Ostwald ripening in emulsions. *Adv. Colloid Interface Sci.* **75** (2), 107–163.

THIELE, U. 2014 Patterned deposition at moving contact lines. *Adv. Colloid Interface Sci.* **206**, 399–413.

THIELE, U., MERTIG, M. & POMPE, W. 1998 Dewetting of an evaporating thin liquid film: heterogeneous nucleation and surface instability. *Phys. Rev. Lett.* **80**, 2869–2872.

THIELE, U., VELARDE, M. G. & NEUFFER, K. 2001*a* Dewetting: film rupture by nucleation in the spinodal regime. *Phys. Rev. Lett.* **87**, 016104.

THIELE, U., VELARDE, M. G., NEUFFER, K. & POMEAU, Y. 2001*b* Film rupture in the diffuse interface model coupled to hydrodynamics. *Phys. Rev.* E **64**, 031602.

THOMPSON, C. V. 1990 Grain growth in thin films. *Annu. Rev. Mater. Sci.* **20** (1), 245–268.

THOMPSON, C. V. 2012 Solid-state dewetting of thin films. *Annu. Rev. Mater. Res.* **42** (1), 399–434.

VOORHEES, P. W. 1985 The theory of Ostwald ripening. *J. Stat. Phys.* **38** (1–2), 231–252.

VRIJ, A. 1966 Possible mechanism for the spontaneous rupture of thin, free liquid films. *Discuss. Faraday Soc.* **42**, 23–33.

WAGNER, C. 1961 Theorie der Alterung von Niederschlägen durch Umlösen (Ostwald-Reifung). *Zeitschrift für Elektrochemie, Berichte der Bunsengesellschaft für physikalische Chemie* **65** (7–8), 581–591.

WEIJS, J. H., MARCHAND, A., ANDREOTTI, B., LOHSE, D. & SNOEIJER, J. H. 2011 Origin of line tension for a Lennard-Jones nanodroplet. *Phys. Fluids* **23** (2), 022001.

WEINSTEIN, S. J. & RUSCHAK, K. J. 2004 Coating flows. *Annu. Rev. Fluid Mech.* **36** (1), 29–53.

WIJSHOFF, H. 2010 The dynamics of the piezo inkjet printhead operation. *Phys. Rep.* **491** (4–5), 77–177.

WILLIAMS, M. B. & DAVIS, S. H. 1982 Nonlinear theory of film rupture. *J. Colloid Interface Sci.* **90** (1), 220–228.

WILLIS, A. M. & FREUND, J. B. 2009 Enhanced droplet spreading due to thermal fluctuations. *J. Phys.: Condens. Matter* **21** (46), 464128.

WITTKOWSKI, R., TIRIBOCCHI, A., STENHAMMAR, J., ALLEN, R. J., MARENDUZZO, D. & CATES, M. E. 2014 Scalar ϕ^4 field theory for active-particle phase separation. *Nat. Commun.* **5**, 4351.

WOEHL, T. J., PARK, C., EVANS, J. E., ARSLAN, I., RISTENPART, W. D. & BROWNING, N. D. 2014 Direct observation of aggregative nanoparticle growth: kinetic modeling of the size distribution and growth rate. *Nano Lett.* **14** (1), 373–378.

WU, L., DONG, Z., KUANG, M., LI, Y., LI, F., JIANG, L. & SONG, Y. 2015 Printing patterned fine 3D structures by manipulating the three phase contact line. *Adv. Funct. Mater.* **25** (15), 2237–2242.

WU, Q. & WONG, H. 2004 A slope-dependent disjoining pressure for non-zero contact angles. *J. Fluid Mech.* **506**, 157–185.

https://doi.org/10.1017/jfm.2018.255 Published online by Cambridge University Press

WYART, F. B. & DAILLANT, J. 1990 Drying of solids wetted by thin liquid films. *Can. J. Phys.* **68** (9), 1084–1088.

XIA, Y. & WHITESIDES, G. M. 1998 Soft lithography. *Annu. Rev. Mater. Sci.* **28** (1), 153–184.

XIE, R., KARIM, A., DOUGLAS, J. F., HAN, C. C. & WEISS, R. A. 1998 Spinodal dewetting of thin polymer films. *Phys. Rev. Lett.* **81**, 1251–1254.

YAMAMOTO, D., NAKAJIMA, C., SHIOI, A., KRAFFT, M. P. & YOSHIKAWA, K. 2015 The evolution of spatial ordering of oil drops fast spreading on a water surface. *Nat. Commun.* **6**, 7189.

YEH, E. K., NEWMAN, J. & RADKE, C. J. 1999 Equilibrium configurations of liquid droplets on solid surfaces under the influence of thin-film forces. Part I. Thermodynamics. *Colloids Surf.* A **156** (1–3), 137–144.

YIANTSIOS, S. G. & DAVIS, R. H. 1991 Close approach and deformation of two viscous drops due to gravity and van der Waals forces. *J. Colloid Interface Sci.* **144** (2), 412–433.

YOUNG, T. 1805 An essay on the cohesion of fluids. *Phil. Trans. R. Soc. Lond.* **95**, 65–87.

YU, T. S., BULOVIĆ, V. & HOSOI, A. E. 2013 Coarsening and solidification via solvent-annealing in thin liquid films. *J. Fluid Mech.* **723**, 69–90.

ZENG, H., ZHAO, B., TIAN, Y., TIRRELL, M., LEAL, L. G. & ISRAELACHVILI, J. N. 2007 Transient surface patterns during adhesion and coalescence of thin liquid films. *Soft Matter* **3**, 88–93.

https://doi.org/10.1017/jfm.2018.255 Published online by Cambridge University Press